

Laboratory observations of gravity-capillary waves under transient wind forcing

B. Mete Uz,¹ Tetsu Hara,² Erik J. Bock,³ and Mark A. Donelan^{4,5}

Received 18 September 2000; revised 27 September 2002; accepted 30 September 2002; published 26 February 2003.

[1] Laboratory experiments were conducted to investigate the response of short wind waves (wave numbers between 50 and 800 rad m⁻¹) under transient wind forcing. Three-dimensional wave number frequency spectra of gravity-capillary waves were measured using a scanning laser slope gauge (SLSG). When wind is started rapidly, gravity-capillary waves of a particular wave number (initial wavelets) first appear, and they are immediately followed by waves over a wider wave number range (both in magnitude and in direction). These waves all appear to grow exponentially, with each wave number growing at its own growth rate. The observed energy input rates from wind to waves are always maximum for along-wind waves and are smaller for waves in directions oblique to the wind. When wind speed is modulated periodically in time, the modulation of the wind stress lags behind that of the wind speed, and the short wind wave spectra lag further behind the wind stress. Assuming that waves are modulated according to existing relaxation theory and that the relaxation rate is identical to the wave growth rate, very short wind waves appear to respond to the instantaneous wind speed while longer wind waves appear to respond to the instantaneous wind stress. **INDEX TERMS:** 4560 Oceanography: Physical: Surface waves and tides (1255); 4506 Oceanography: Physical: Capillary waves; 4504 Oceanography: Physical: Air/sea interactions (0312); **KEYWORDS:** gravity-capillary waves, surface waves, wind waves, capillary waves

Citation: Uz, B. M., T. Hara, E. J. Bock, and M. A. Donelan, Laboratory observations of gravity-capillary waves under transient wind forcing, *J. Geophys. Res.*, 108(C2), 3050, doi:10.1029/2000JC000643, 2003.

1. Introduction

[2] There has been increasing interest in ocean surface waves in the gravity-capillary range, because these waves enable microwave remote sensing of ocean surface roughness and are correlated with the air-sea fluxes of mass, momentum and energy. Yet, our current understanding of the dynamics of short wind waves is far from adequate. Past studies have been mostly limited to two simple conditions: (1) the initial generation of short wind waves and (2) the saturation spectrum of short wind waves under stationary and homogeneous wind forcing. The processes between the initial generation and the final saturation, as well as the wave dynamics under nonstationary and/or nonhomogeneous wind forcing are not well researched or reported.

1.1. Initial Generation of Short Wind Waves

[3] Early studies of surface waves mostly focused on the initial generation of waves. One of the most important experiments was done by *Kawai* [1979], who showed that the earliest detectable wave field was dominated by gravity-capillary waves of a particular frequency called initial wavelets and that the growth of the “initial wavelets” was exponential (with a constant growth rate) over a period of time. He defined the growth rate β_g as

$$\beta_g = \frac{1}{S} \frac{\partial S}{\partial t} \quad (1)$$

under spatially homogeneous conditions, where S is the wave amplitude (or slope) spectrum and t is time. When the amplitude of these initial wavelets is small enough, wave breaking and nonlinear interactions between waves of different scales can be neglected. Then, the energy balance is simplified such that the observed growth rate β_g is the difference between the rate of energy input β_w from wind to waves and the viscous energy dissipation rate of waves,

$$\beta_g = \beta_w - 4\nu k^2 \quad (2)$$

where ν is the viscosity of water and k is the wave number. Based on this idea, *Kawai* [1979] also developed a model of wave growth as a shear instability in order to explain the observed exponential growth of the initial wavelets. Shortly before *Kawai's* [1979] experiments, *Larson and Wright*

¹Earth System Science Interdisciplinary Center, University of Maryland, College Park, Maryland, USA.

²Graduate School of Oceanography, University of Rhode Island, Narragansett, Rhode Island, USA.

³Interdisciplinary Center for Scientific Computing, University of Heidelberg, Heidelberg, Germany.

⁴Rosenstiel School of Marine and Atmospheric Science, University of Miami, Miami, Florida, USA.

⁵Also at National Water Research Institute, Canada Centre for Inland Waters, Burlington, Ontario, Canada.

[1975] used a microwave radar to observe wave growth at discrete wavelengths in the gravity-capillary range. They were able to make accurate measurements of the early stages of wave growth owing to the extreme sensitivity of microwave backscatter to surface waves and its inherent spatial averaging. They observed periods of exponential growth similar to those reported by *Kawai* [1979]. The major difference between the two studies was that *Larson and Wright* [1975] observed exponential growth at several wave numbers simultaneously, whereas *Kawai* [1979] observed wavelets of a particular wavelength dominating the early growth stage.

1.2. Evolution of the Wave Field

[4] In contrast to the extensive early studies on the initial exponential growth stage, the subsequent nonlinear evolution of the wave field has been poorly investigated. In the early stage of wave growth, the wave field is nearly two-dimensional and consists of long-crested waves traveling in the along-wind direction. However, the advanced stages of wind seas are three-dimensional and there is a significant directional spread of the wave spectrum. The transition from two-dimensional to three-dimensional spectra has been investigated only qualitatively [e.g., *Caulliez and Collard*, 1999]. Of particular interest is the energy input rate from wind to waves propagating at oblique angles with respect to the wind. This is an important parameter in estimating the drag coefficient by integrating the wave-induced stress supported by waves in all directions [e.g., *Makin and Kudryavtsev*, 1999; *Uz et al.*, 2002]. Commonly used parameterizations for the wind input rate have simple cosine dependence on the wind wave angle such that

$$\beta_w(\theta) = \beta_w(\theta = 0)\cos^p \theta \quad (3)$$

where p is some empirical number and θ is the angle between wind and wave propagation directions. The cosine function is merely a convenient functional form that equals one in the along-wind direction and goes to zero at 90° . The numerical value of the power p is largely unknown.

[5] Another important characteristic of the evolution of the wave field is the “frequency downshift,” as pointed out by *Kawai* [1979] and others. After the initial wavelets of a particular frequency reach a certain magnitude, the peak frequency of the spectrum starts to migrate to lower frequencies; hence, progressively longer waves come to dominate the wave field. *Janssen* [1986] proposed a theory of the period doubling of gravity-capillary waves as a result of the combination of wind input and the second harmonic resonance. His theory agreed qualitatively with previous observations, but its validity has not been fully established because no quantitative observations have been performed beyond the initial exponential growth stage.

1.3. Modulation of Short Wind Waves

[6] Although the spectra of short wind waves under stationary and homogenous wind forcing (saturation spectra) have been investigated extensively both in laboratories [e.g., *Jähne and Riemer*, 1990; *Hwang et al.*, 1993; *Zhang*, 1995; *Hara et al.*, 1997] and in situ [e.g., *Hara et al.*, 1994, 1998; *Hwang et al.*, 1996], the response of short wind waves to varying wind forcing has not been studied as

extensively through direct observations. The importance of the wind gustiness on the overall air–sea fluxes was discussed by *Dorman and Mollo-Christensen* [1973] based on their field observations, while *Weissman et al.* [1996] investigated the response of microwave cross section of the sea to wind fluctuations and found very weak correlation between the wind variability and the cross-section variability. In laboratory setting, *Autard and Caulliez* [1996] investigated the evolution of the wave field under accelerating wind by suddenly varying the wind tunnel section. They observed that very short wind waves responded quickly to the increased wind speed very near the surface, and that the wind stress measured away from the surface responded with significant delay because of the slower turbulent boundary layer development with fetch.

[7] Microwave backscatter from the ocean surface is often modulated by swell and longer gravity waves. Even though a significant part of the backscatter modulation is attributed to geometric effects associated with the Bragg scattering mechanism, there is nevertheless general belief that wave spectra of short wind waves are hydrodynamically modulated by longer waves. There are two possible mechanisms by which long waves can modulate wave spectra at higher wave numbers. The orbital velocity associated with the long waves creates divergence near the trough and convergence near the crest of the waves, and the short wind wave spectra tend to be higher near the convergence zone and lower at the divergence zone. Also, short waves may be modulated if the wind stress affecting the growth of the short waves varies along the profile of the long waves. This effect becomes more important if the response timescale (relaxation timescale) of the short waves to varying wind stress is shorter than the period of the long waves. In addition to swell and longer gravity waves, short wind waves can be modulated by near surface currents (e.g., divergence/convergence due to internal waves) and wind variability (gustiness). Understanding how short wind waves respond to nonstationary and/or nonhomogeneous wind forcing is particularly important to interpret microwave backscatter signals from the ocean surface. This interpretation will allow better estimates of surface gravity waves, internal waves, currents, and coherent atmospheric structures from the modulated part of the backscatter signals.

[8] The response of a wave spectral component to fluctuating wind input is usually characterized by a parameter called the “relaxation rate.” The relaxation rate is defined as a rate at which the spectrum returns to saturation after an infinitesimal perturbation of the wind forcing is introduced. The relaxation rate is theoretically identical to the initial wave growth rate under a set of assumptions [e.g., *Hara and Plant*, 1994], and therefore the relaxation rate is often replaced by the growth rate in numerical modeling of the wave modulation. However, the validity of the assumptions associated with the relaxation theory as well as the exact value of the relaxation rate has not been examined systematically using observational data.

1.4. Laboratory Studies of Short Wind Waves Under Transient Wind Forcing

[9] In this paper we analyze short wind wave data (wave numbers between 50 and 800 rad m^{-1}) collected in a wind wave flume using a scanning laser slope gauge (SLSG), an

instrument capable of obtaining three-dimensional wave number frequency spectra at a temporal resolution of a few seconds under time-transient wind forcing. After presenting the experimental method (section 2), we report the observations of the wave field after an abrupt start of the wind, as the initial long-crested wavelets evolve to the final saturation form with significant directional spreading (section 3). We then investigate the response of short wind waves to periodically modulated wind forcing in section 4. The periodic wind modulation allows us to perform phase averaging over multiple modulation periods as a proxy for ensemble averaging. Finally, the concluding remarks are given in section 5.

[10] In this paper, we treat the wind forcing as a given (controlled) variable and focus on the response of short wind waves. In reality, however, wind and wind waves are coupled with bidirectional causal relationships. Wind forcing modifies waves, but the waves in turn enhance the wind stress by increasing the effective surface roughness. The impact of the wave spectrum on the wind stress and the drag coefficient is studied in a companion paper [Uz *et al.*, 2002].

2. Experimental Methods

2.1. Overview

[11] The experiments were performed in the Gas Transfer Flume (32.6 m length, 0.76 m width and 0.85 m height) at Canada Centre for Inland Waters (CCIW) in 1993 and 1996. The tank was filled with fresh water to a 0.25 m depth. The air side of the tank was completely sealed, and the air blown over the water surface circulated back to the fan through a return duct. This feature allowed the air to reach a steady state with regard to temperature and humidity so that the secondary motion in water due to evaporative cooling was minimized. At the air inlet, a honeycomb screen provided uniform, horizontal airflow. The air–water flow entrance junction consisted of an adjustable floor hinged to bring the airstream smoothly on to the water surface. During the experiments, the floor was tilted downwards at an angle of 5° from a hinge at 0.483 m from the downwind edge of the floor. At the downwind edge, the surface of the floor was 0.04 m above the water surface. The adjustable floor was aluminum plate with raised diamonds to provide “nonskid” properties for walkways. This roughness stimulated growth of a turbulent boundary layer in the air before it attached to the water surface. At the downwind end of the tank, a shallow beach was installed to absorb wave energy and minimize wave reflections.

[12] Wind was generated by a computer-controlled fan that allowed the wind speed to be varied in an arbitrary way. Two schemes were studied: an rapidly starting wind and a periodically modulated wind. The experiments with rapidly starting wind allowed observations of wave evolution from generation to saturation. In order to simulate wind gustiness in a repeatable fashion, wind speed was periodically modulated with a modulation amplitude of 15–50% of the mean wind speed and with a period of 10 or 20 s. The results under steady wind have been reported by Hara *et al.* [1997] and are not repeated here.

2.2. Wind Measurements

[13] Wind measurements were made with a hot-film anemometer at 14 m fetch and at a fixed height of 0.1 m

above the mean water surface in all cases. In addition, measurements were made at different heights in selected cases. In the rest of the paper, wind speeds are reported at the same height of 0.10 m. The probe was calibrated in a small wind tunnel before and after the experiment. The angle of attack was varied from -40° to 40° , and the wind speed was varied between 0.79 and 12.6 m s^{-1} . The calibrations before and after the experiments were nearly identical. The same calibration was therefore used for the entire data set. The mean wind speed measurements from the hot-film probe were also compared against Pitot tube measurements for further assurance.

[14] The method of estimating the wind stress at the water surface is discussed in detail by Uz *et al.* [2002] with supporting figures. Therefore, we summarize only the salient points here. Under rapidly starting wind, the wind stress at the sensor height was estimated using a modified cospectrum method. We calculated the cospectrum up to a cutoff period T_c (i.e., the period of the largest eddies resolved) and extrapolated the contribution from larger eddies (above T_c) using an empirically determined form of the cospectrum. The cutoff period T_c was chosen to be 2 s. We estimated that the error introduced by this method was less than 5%. When the wind forcing was periodically modulated, the horizontal/vertical wind velocity was decomposed into the phase average (averaged at the same phase over multiple periods of forcing) and the turbulent fluctuation. Then, the stress estimate was obtained by multiplying the horizontal and vertical turbulent fluctuations and averaging the result over the maximum number of periods available. The stress estimate was further running averaged over 1 s centered at a particular phase. The vertical stress profile was measured for various steady wind speeds and was found to be linear. When wind forcing was not stationary, the wind stress profile was still found to be linear except inside the thin boundary layers where the wind velocity significantly differed from the mean. This approximate linearity of the stress profile enabled us to extrapolate the stress from the 0.1 m height to the surface. The only difference introduced by the unsteadiness was that the vertical stress gradient was not a constant but a function of time. Therefore, we used the measured wind stress at the 0.1 m height and the estimated wind stress at the ceiling (0.6 m above the water surface) in order to determine the stress gradient. The relationship between the wind stress at the ceiling and the wind speed at the 0.1 m height was obtained empirically from a series of direct wind stress measurements at several different heights at various wind speeds.

[15] In the following sections, we always report the estimated wind stress values at the water surface.

2.3. Wave Measurement

[16] Wave measurements were made with a SLSG developed by Bock and Hara [1995] at a fixed fetch of 13 m. This instrument measures surface slope both in time and in space so that complete three-dimensional wave number frequency spectra can be estimated. Since the design details of the instrument have been explained in two papers [Bock and Hara, 1995; Hara *et al.*, 1997], only the salient features of the instrument are given here.

[17] The SLSG consists of two units. A laser pod, placed just below a glass window at the bottom of the tank,

generates a vertical laser beam that scans a circle of 0.15 m diameter at the water–air interface. An overhead unit, placed just above a glass window at the ceiling of the tank, captures the angle of the beam after it is refracted at the interface. From the angle of refraction, the head unit calculates the instantaneous slope of the water surface in two orthogonal components. This calculation is performed at 129 locations along the scan circle for spatial information, and successive scans at 69.4 Hz (436 rad s^{-1}) provide temporal information. The stream of surface slope measurements from the SLGS is then processed to estimate the three-dimensional frequency wave number slope spectrum $S(k, \theta, \omega)$, which is defined for $0 < k < \infty$, $-\frac{\pi}{2} < \theta < \frac{\pi}{2}$, and $-\infty < \omega < \infty$. Here ω is the angular frequency, k is the magnitude of the wave number and θ is the angle between the wave propagation direction and the wind direction. The two-dimensional wave number spectrum $S(k, \theta)$ is obtained by integrating $S(k, \theta, \omega)$ in ω , and the one dimensional (omnidirectional) wave number spectrum $S(k)$ is calculated by integrating $S(k, \theta)$ in θ . The optimal wave number resolution has been estimated to be 25 rad m^{-1} , that is, an estimated spectrum at a particular wave number is effectively the average of the true spectrum over a $\pm 12.5 \text{ rad m}^{-1}$ range. The thickness of the scanning laser beam limits the highest measurable wave number to be approximately 1000 rad m^{-1} . In time domain, a 1.84 s wide Hanning window has been applied before each Fourier transform. Therefore, the smallest time resolution we may achieve is about 1 s. Since the instrument has been designed for field operations, the noise level of the instrument is relatively high compared with simpler laboratory-based instrument. For example, when the wind is rapidly started over a flat surface, the SLGS can detect the initial wavelets when their root mean square slope exceeds about 0.005, which corresponds to wave amplitude of roughly 0.03 mm for wave number 200 rad m^{-1} . This relatively high detection threshold limits our observation of the very early stage of the wave generation, as discussed in the next section.

[18] In order to obtain statistically significant estimates of the spectra it is necessary to take sufficient averaging. For the steady wind experiments, the confidence level was determined empirically, and time averaging over 5–10 min was found to be adequate (95% confidence level of roughly $\pm 1 \text{ dB}$) for the three dimensional spectra [Hara *et al.*, 1997]. For the transient wind experiments, different averaging methods were used to optimize the resolution in frequency and wave number as well as the statistical stability. They are explained in section 3. The confidence level (degree of freedom) of the results was determined empirically throughout this study.

3. Rapidly Starting Wind

[19] The main purpose of this section is to present detailed observations of the evolution of the wave field during and after the exponential growth stage of the initial wavelets. All the experiments were repeated four times and ensemble averaging was used for wind speed, wind stress, and wave spectra. Since the experiment was reproducible within the statistical scatter, only the results of ensemble averaging are presented. To improve the statistical accuracy, the wind stress measurements were further boxcar averaged

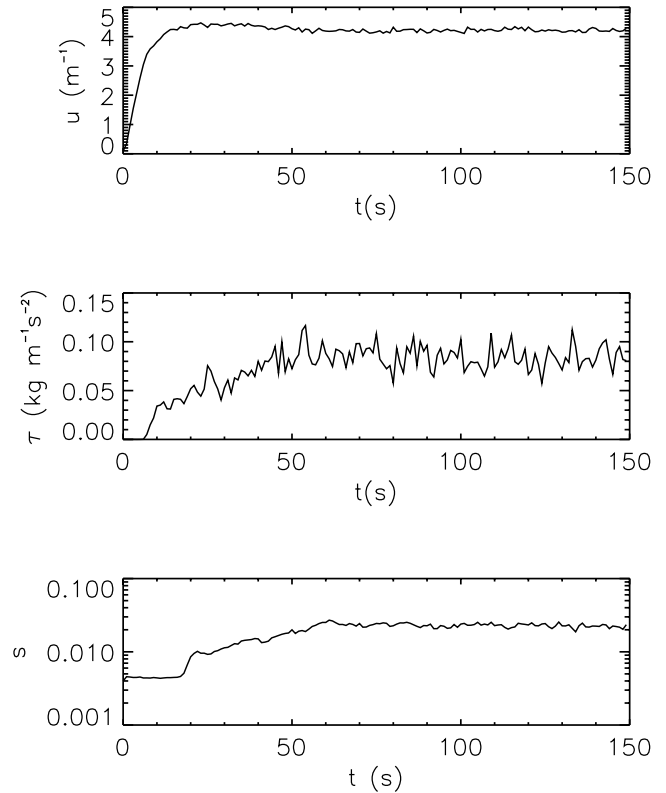


Figure 1. Time series of ensemble-averaged wind speed (upper panel), wind stress (middle panel), and mean square slope (lower panel) for abruptly starting wind of 4.5 m s^{-1} .

over 4 s, yielding the 95% confidence level of about $\pm 10\%$. Our measurements of the wave growth at high winds were not reliable because the wave growth occurred over a very short period after the wave signal exceeded the noise level of the SLGS. We therefore present the results at a relatively low wind condition (wind speed 4.5 m s^{-1}) in this section.

[20] We define $t = 0$ as the instant when the fan was turned on. The time series of ensemble-averaged wind speed (u), wind stress (τ), and mean square slope (s) are shown in Figure 1. Because of the inertia in the system, wind speed does not develop instantaneously, but it reaches about 80% of its final value at $t = 10 \text{ s}$. (We believe that this delayed response of the fan helped suppressing the generation of seiche in the tank as reported by Melville *et al.* [1998], since we did not observe any appreciable seiche during the rapidly starting wind experiments.) Wind stress starts to increase after a small delay, during which the turbulent boundary layer grows to the measurement height. After the hot-film probe is well within the turbulent boundary layer, the stress reaches the first plateau ($t = 10\text{--}18 \text{ s}$). This plateau value is roughly consistent with the turbulent stress value over a smooth surface. Once the waves appear around $t = 18 \text{ s}$, the wind stress starts to increase again, and the waves and wind stress both reach the final steady state at about $t = 60 \text{ s}$. More details of the time evolution of wind stress are discussed in a companion paper [Uz *et al.*, 2002].

3.1. Fetch Dependence

[21] Since our observations continue for rather long time periods, it is useful to clarify the fetch dependence of the

observed wave field. Strictly speaking, the wave field at a particular location is fetch independent up to the instant when the fastest waves from the upwind edge of the tank have arrived. If the nonlinear wave–wave interaction is negligible, each wave number component may be considered independently. Then, each wave number component can be assumed fetch independent and time dependent until the arrival of the first waves of the particular wave number from the upwind edge. After that time, this wave component remains at the same stage of development (fetch limited and time independent), because waves that arrive later at this location will have experienced the same amount of wind forcing since their generation at the upwind end of the tank. For example, gravity waves with a wave number of 35 rad m^{-1} travel at a group speed of 0.3 m s^{-1} . It therefore takes approximately 40 s for this wave number component to change from fetch independent to fetch limited at the 13 m fetch. For shorter waves of 70 rad m^{-1} traveling at 0.20 m s^{-1} it takes about 65 s to become fetch limited. The group speed of very short gravity-capillary waves (wave numbers larger than 450 rad m^{-1}) exceeds 0.3 m s^{-1} and therefore they change from fetch independent to fetch limited in less than 40 s. However, because of their fast response timescale to wind input and dissipation, they are not likely to retain information about the upwind edge by the time they reach the 13 m fetch. Hence, the wave field of such short waves remains fetch independent at all times at the 13 m fetch.

[22] Of course, the nonlinear wave–wave interaction is not entirely negligible and the above statement is not strictly applicable. Even if very short waves have very fast response timescale to wind and dissipation, they may still exhibit weak fetch dependence because they interact with longer waves that are fetch dependent. In particular, parasitic capillaries that are formed near the crest of gravity waves are expected to be strongly fetch dependent.

3.2. Evolution of Waves in Wind Direction

[23] Since the wave field is mostly one-dimensional (long-crested) at early stages of the wave development, we first present the evolution of the three-dimensional wave number frequency spectrum $S(k, \theta, \omega)$ in the wind direction ($\theta = 0$) for a wind speed of 4.5 m s^{-1} in Figure 2. Here, in order to reduce the statistical scatter, the spectrum was boxcar averaged over 6 s. In all figures, the theoretical dispersion relation is shown by a solid line and two Doppler-shifted dispersion relation curves (dotted lines) are added corresponding to vertically uniform currents of 0.05 and 0.1 m s^{-1} . In addition, the frequency spectrum $S(\omega)$ and the along-wind wave number spectrum $S(k, \theta = 0)$ are calculated for each panel and the results are shown in Figures 3 and 4.

[24] Waves are first detected by the SLSG approximately 15 s after the onset of wind (Figure 2a). The location of the peak of the spectrum is about wave number $200\text{--}250 \text{ rad m}^{-1}$ and frequency $70\text{--}100 \text{ rad s}^{-1}$, roughly along the dispersion relation with a 0.05 m s^{-1} current. The wind friction velocity at this stage fluctuates between 0.15 and 0.19 m s^{-1} . Our values of the friction velocity and the frequency of the initial wavelets are roughly consistent with Kawai's [1979] observation. He reported that the frequency of the initial wavelets at friction velocity 0.17 m s^{-1} was about 90 rad s^{-1} .

[25] These initial wavelets are quickly followed by other wave numbers and the spectrum becomes broad by $t = 18 \text{ s}$, as shown in Figure 2b. This observation suggests that at an early stage of the wave generation waves over a wide wave number range grow simultaneously and independently, and that the initial wavelets first appear simply because their growth rate is the largest. This view is further confirmed later in this section. The peak wave energy is located near the dispersion relation with a 0.05 m s^{-1} current at lower wave numbers but is rather close to the curve with a 0.1 m s^{-1} current at higher wave numbers. This shows that the near surface drift current is strongly sheared and shorter waves are more affected by the current. By $t = 24 \text{ s}$ energy spreads almost over the entire wave number domain and the peak frequency/wave number appears to be slightly downshifted (Figure 2c).

[26] There is a sudden transition from $t = 24$ to $t = 27 \text{ s}$ (Figure 2d). Up to $t = 24 \text{ s}$ the spectrum is rather broad, but by $t = 27 \text{ s}$ a clear spectral peak at wave number 170 rad m^{-1} and frequency 50 rad s^{-1} is established. This does not appear to be the result of the “period doubling” as suggested by Janssen [1986], since the peak wave number at the initial stage, located at wave number $200\text{--}250 \text{ rad m}^{-1}$, is much less than twice the wave number of the new peak. This spectral peak continues to grow and slowly downshift in frequency/wave number.

[27] Starting at around $t = 36 \text{ s}$ (Figure 2e) and becoming clearer by $t = 51 \text{ s}$ (Figure 2f) is the emergence of the bound waves. Bound waves are the higher Fourier harmonics of the steep dominant waves appearing in the wave number frequency spectral analysis. They are phase locked to the dominant waves instead of propagating independently at their own phase speed. In order to distinguish the bound waves from the free waves, the propagation speed of the dominant waves is indicated by dashed lines in Figures 2e–2g. First, the frequency of the dominant waves has been determined for each panel from the frequency spectrum, and their propagation speed has been estimated using the dispersion relation and assuming two different mean currents of 0 and 0.05 m s^{-1} .

[28] The second harmonics of the spectral peak is clearly visible at $t = 36 \text{ s}$ centered around $250\text{--}300 \text{ rad m}^{-1}$ corresponding to the dominant wave peak near $125\text{--}150 \text{ rad m}^{-1}$. As the wave field matures, progressively longer waves dominate the wave field, and the presence of higher bound harmonics becomes evident by $t = 51 \text{ s}$. By this time the bound waves have much higher frequencies than the free waves, as indicated by the separation of the dashed lines from the dotted lines, and it is easier to distinguish the bound waves from the free waves. It is also noteworthy that the free waves at high wave numbers have been significantly reduced from $t = 36$ to 51 s . At the final stationary stage (Figure 2g) the separation between the bound wave mode and free wave mode is evident with almost comparable wave energy in each wave mode.

[29] The time series of the along-wind wave number spectrum $S(k, \theta = 0)$ during the development of the wave field is shown in Figure 5. To reduce the statistical noise the spectra have been averaged over the wave number ranges described in the figure caption. Wave numbers roughly between 150 and 500 rad m^{-1} all appear within a couple

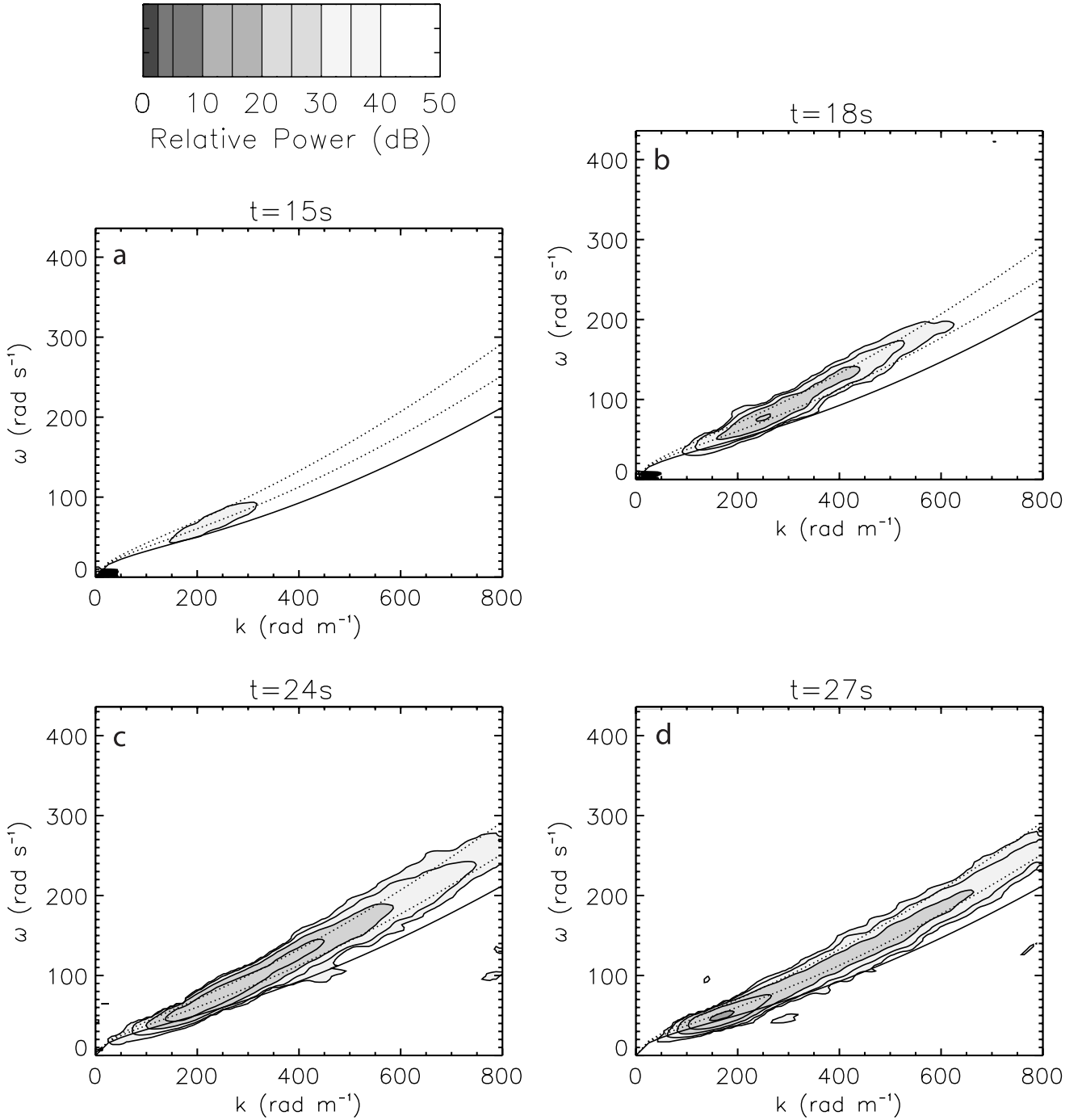


Figure 2. Along-wind wave number frequency spectrum averaged over 6 s centered around the time specified over the panel for abruptly starting wind of 4.5 m s^{-1} . Solid line, dispersion relation without Doppler shift. Dotted lines, dispersion relations Doppler shifted by mean current of 0.05 and 0.10 m s^{-1} . After bound waves emerge, dashed lines are added to represent the phase speed of the dominant waves Doppler shifted by mean current of 0 and 0.05 m s^{-1} .

of seconds of each other and grow exponentially first. This observation further supports the view that waves over a relatively wide range of wave numbers are generated simultaneously and grow independently at their own initial growth rates, and that the initial wavelets observed by Kawai [1979] are indeed the wave component with the largest growth rate. All wave components grow first, hit

their maximum, and then gradually decrease, exhibiting the well-known “overshooting” phenomena.

3.3. Evolution of Waves in Oblique Directions Relative to Wind

[30] Even though the airflow in the wind wave tank is very nearly one-dimensional, waves at oblique directions

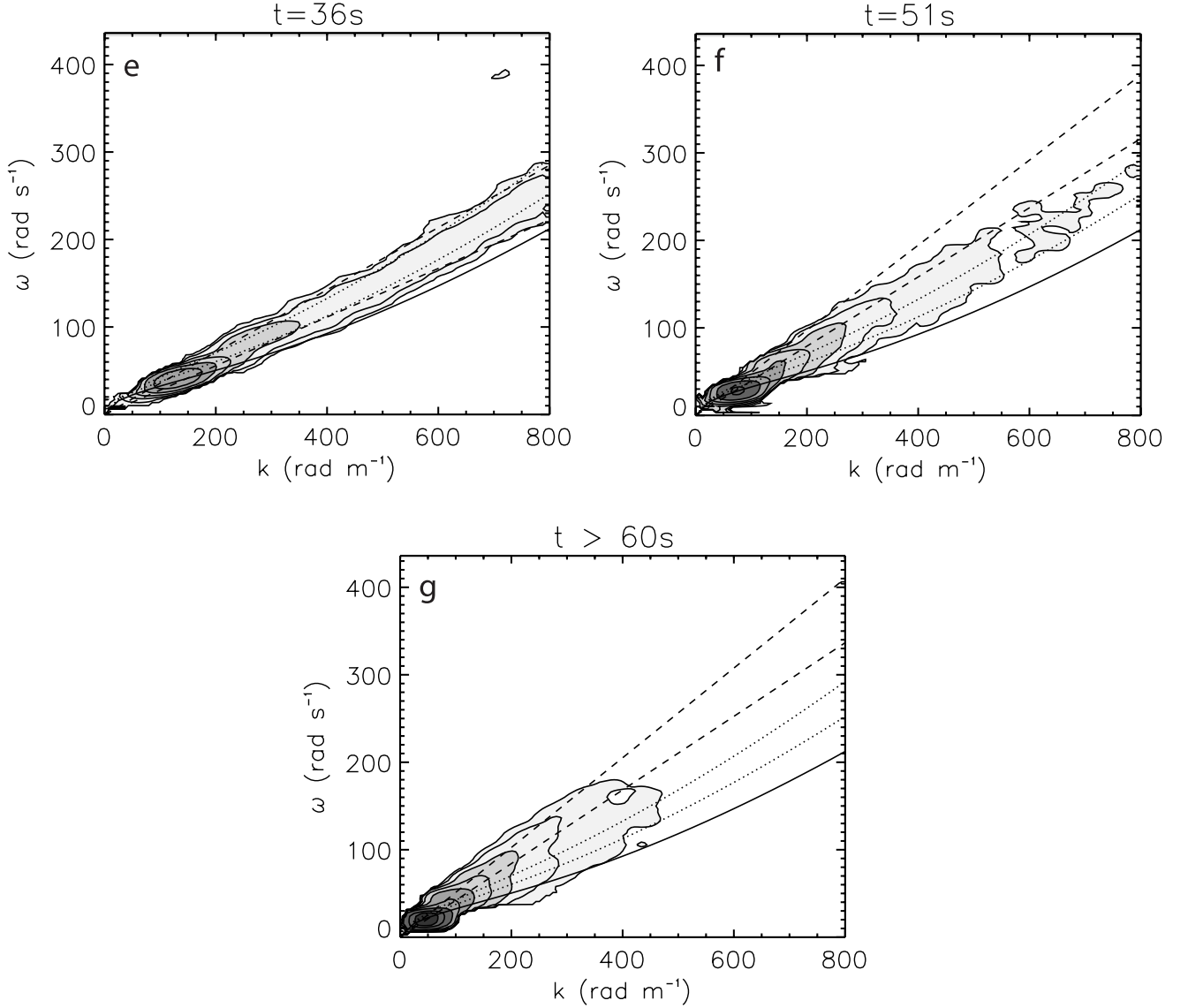


Figure 2. (continued)

are still generated. It is of interest to examine how these oblique waves receive energy and grow. One possible scenario is that the oblique waves are initially generated in the same manner as the along-wind waves but with smaller growth rates, and therefore they become visible at later times. The initial disturbances are not likely to have any directional preference. All these disturbances, except those exactly perpendicular to the wind, experience a component of the wind normal to them, and thus are possibly subject to energy input from the wind. Alternatively, waves in oblique directions may receive energy predominantly through the nonlinear wave interaction rather than the direct input from the wind.

[31] In Figure 6, we show the time series of the wave number slope spectrum $S(k, \theta)$ at four different directions. In order to reduce the statistical noise, the spectrum is averaged over $\pm 15^\circ$. For example, the results for 60° are actually the average between 45° and 75° from the wind direction. Because of the relatively high noise level of the instrument we may not observe the initial wave growth over a wide dynamic range. Nevertheless, in general the initial wave

growth appears to be exponential and take place almost simultaneously at all four directions at all wave numbers. At very high and very low wave numbers and at large angles relative to the wind, the growth seems to start with some delay, but this may be simply because the early part of the growth is obscured by the noise floor. As expected, along-wind waves grow fastest and the growth rate decreases with increasing angle to the wind. The tendency of overshoot is also the strongest for along-wind waves.

3.4. Initial Wave Growth Rate

[32] Even though wave growth may start very soon after the onset of wind forcing, wave energy is not immediately detectable by the SLSG. Therefore, our measurements are not as suitable for the study of the initial growth rate as the pioneering measurements by *Larson and Wright* [1975] and by *Kawai* [1979], who used very sensitive instruments to observe the very early stage of the exponential wave growth over a few decades with single point frequency measurements. The advantage of our instrument, on the other hand, is that it can capture the directional wave number spectrum

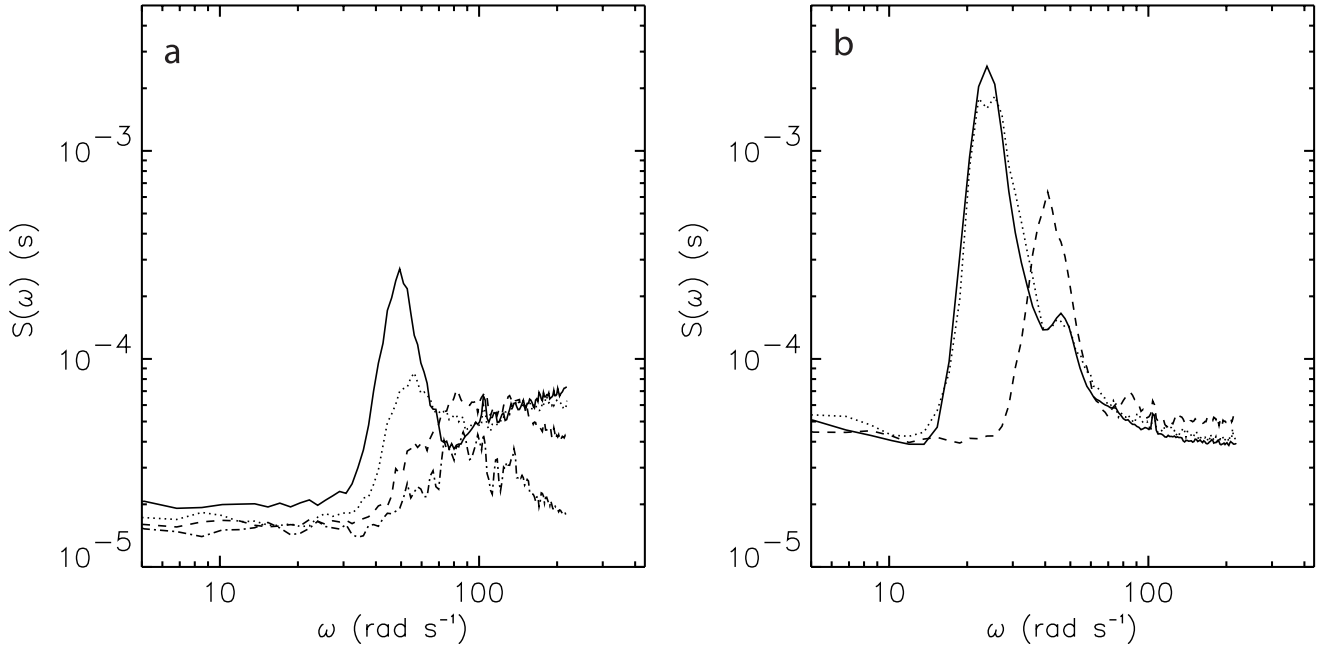


Figure 3. Evolution of frequency slope spectrum. Wind speed is 4.5 m s^{-1} . (a) Dash-dot $t = 15 \text{ s}$, dash $t = 18 \text{ s}$, dotted $t = 24 \text{ s}$, and solid $t = 27 \text{ s}$. (b) Dash $t = 36 \text{ s}$, dotted $t = 51 \text{ s}$, and solid $t > 60 \text{ s}$.

directly. Since the time series of the wave number spectrum in oblique directions (Figure 6) indicate that the initial exponential wave growth seems to occur at different directions simultaneously, it is of interest to quantify the initial growth rate and examine its directional dependence.

[33] Using the time series of the directional wave number slope spectrum plotted in linear-log coordinates, we estimate the initial growth rate for each case separately, by first visually determining the exponential growth range in time, that is, from the instant the wave signal exceeds the noise level to the time the wave growth begins to slow down, and

then best fitting a straight line to the data. Since the determination of the exponential growth stage is somewhat subjective, we use several different criteria and determine the possible range of the growth rate instead of a single value. The result is not shown if the exponential growth is observed over less than 1 order of magnitude. The determination of the friction velocity during the initial wave growth is also nontrivial, since it also depends on the definition of the exponential growth stage. Therefore, we present the possible range of the friction velocity instead of a single value.

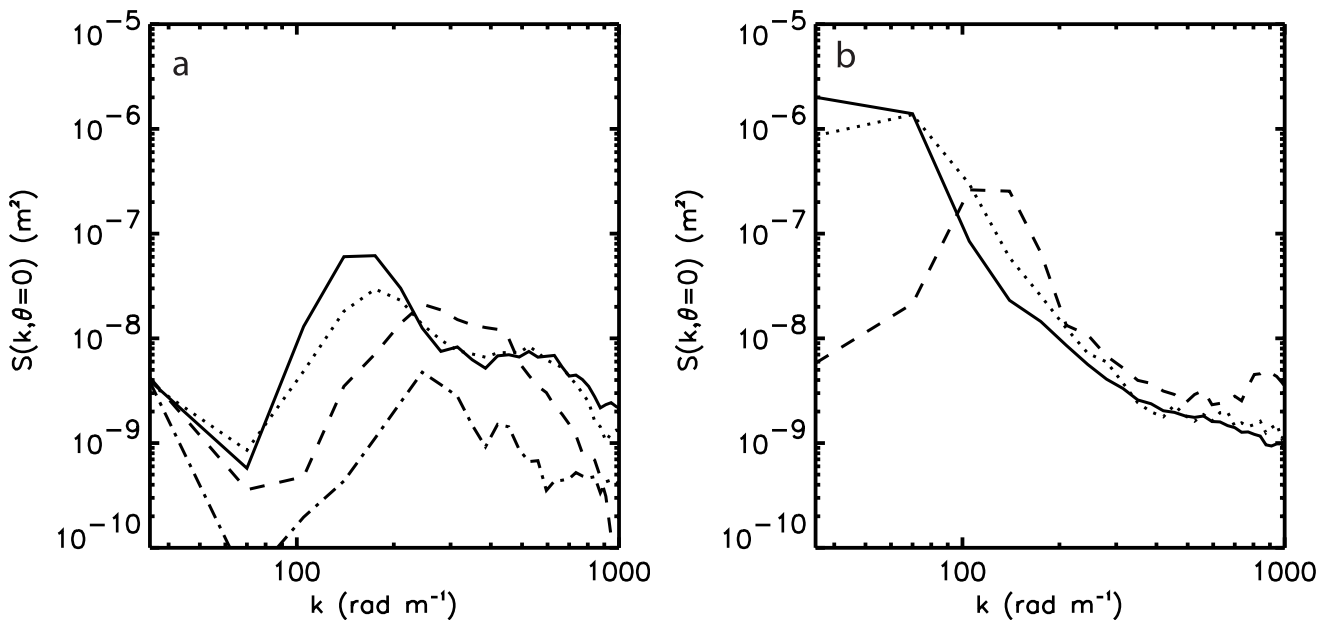


Figure 4. Evolution of along-wind wave number slope spectrum. Wind speed is 4.5 m s^{-1} . (a) Dash-dot $t = 15 \text{ s}$, dash $t = 18 \text{ s}$, dotted $t = 24 \text{ s}$, and solid $t = 27 \text{ s}$. (b) Dash $t = 36 \text{ s}$, dotted $t = 51 \text{ s}$, and solid $t > 60 \text{ s}$.

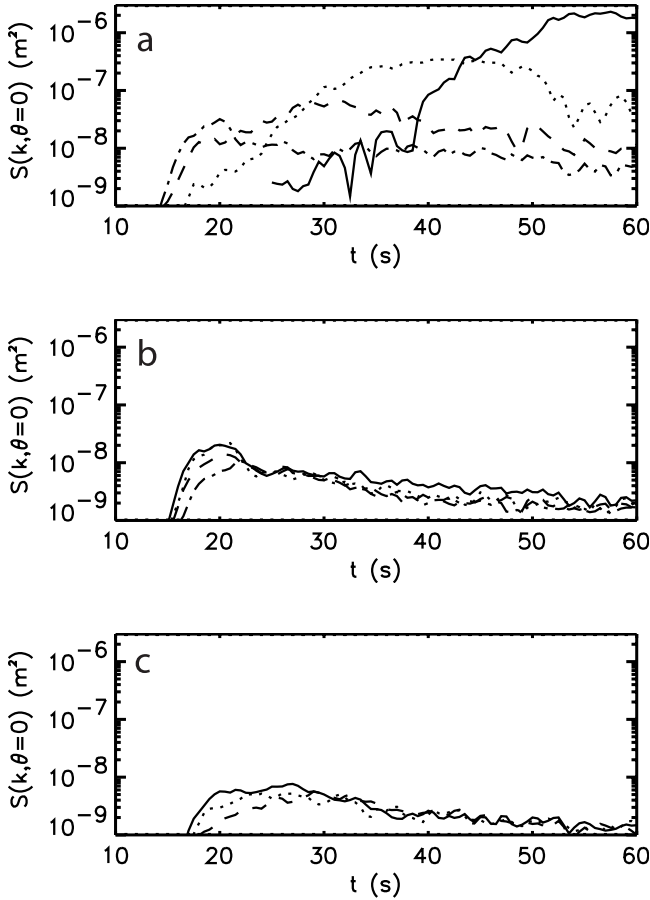


Figure 5. Time series of along-wind wave number slope spectrum. Wind speed is 4.5 m s^{-1} . The spectrum is integrated over the wave number range described below. (a) Solid 35–70, dotted 105–140, dash 175–210, and dash-dot 245–280 rad m^{-1} . (b) Solid 315–350, dotted 385–420, dash 455–490, and dash-dot 525–560 rad m^{-1} . (c) Solid 595–630, dotted 665–700, and dash 735–770 rad m^{-1} .

[34] In Figure 7, crosses indicate our estimated growth rates for along-wind waves at different wave numbers at a wind speed of 4.5 m s^{-1} . The horizontal extent of the crosses indicates the range of wave numbers averaged, and the vertical extent of the crosses indicates the uncertainty of the estimates. The range of the estimated friction velocities is between 0.15 and 0.19 m s^{-1} . Plotted also in the same figure are the measured growth rate of the initial wavelets observed by Kawai [1979] and theoretical estimates of growth rates by Kawai [1979] and van Gastel *et al.* [1985] at a similar wind speed. Note that Kawai [1979] observed the growth rate of only a single wave number component. We cannot compare our results with those by Larson and Wright [1975], since they only reported the friction velocity after the wave field became fully developed.

[35] Our observed growth rates are somewhat lower than Kawai's observation but are consistent with theoretical estimates at the middle three wave number ranges (i.e., wave numbers roughly between 150 and 500 rad m^{-1}). This is the same wave number range where the waves first appear within a couple of seconds of each other (Figure 5). At the lowest wave number range theoretical estimates are not

given. Our observed growth rate at the highest wave number range is significantly higher than the theoretical estimates, suggesting that these waves may receive energy through mechanisms other than direct wind input.

[36] The directionality of the wind input rate (the observed growth rate plus the viscous dissipation rate) is shown in Figure 8, also at a wind speed of 4.5 m s^{-1} . The initial growth rate is first estimated for all wave angles relative to the wind, and is averaged over four directional ranges of $\theta = 0 \pm 15^\circ$, $30 \pm 15^\circ$, $60 \pm 15^\circ$, and $90 \pm 15^\circ$. Then, the viscous dissipation rate is added to the results and the estimated wind input rate is normalized by its along-wind value.

[37] Our results are compared with a simple cosine function form, $\cos^p(\theta)$ with $p = 0.5, 1$, and 2 . Note that the cosine function form has also been averaged over the same four directional ranges and then normalized by its along-wind value for consistency. We here show the wind input rate rather than the growth rate because the former was suggested (or simply assumed) to have a simple cosine function form in previous studies.

[38] The directionality at the lowest and highest wave number ranges (stars, tilted crosses) is significantly weaker than that at the middle three wave number ranges (triangles, diamonds, and squares). Since the along-wind growth rates are found to be consistent with theoretical estimates in the middle three wave number ranges, we focus on the directionality of the wind input rates also in the same range (triangles, diamonds, and squares). There is not a single exponent p , which follows the data adequately. The results at $\theta = 30 \pm 15^\circ$ are close to the $p = 2$ curve and those at $\theta = 60 \pm 15^\circ$ are between the $p = 2$ and $p = 1$ curves. At $\theta = 90 \pm 15^\circ$ the directionality appears to be between the $p = 1$ and $p = 0.5$ curves.

3.5. Discussion

[39] Here, we discuss two effects that may have influenced our observations of the initial wave growth. The first is the slowness of the wind speed increase. As shown in Figure 1, the wind speed does not increase instantly at $t = 0$ s but continues to increase up to about $t = 15$ s. Although the wind speed is almost steady by the time the initial wave growth is observed after $t = 15$ s, it is nevertheless possible that the growth rates are somewhat dependent on the history of wind forcing rather than instantaneous wind forcing. This may explain, at least partially, why our observed growth rates are lower than Kawai's [1979] observation.

[40] The other effect is the presence of sidewalls in the airside of the tank. Although waves propagating in the wind direction always stay in the middle of the tank and feel the maximum wind forcing, waves propagating in oblique directions travel between the two sidewalls and feel reduced wind forcing when they are near the sidewalls, where wind speed itself is reduced. If we assume that the sidewalls are smooth, the mean wind speed across the tank is estimated to be roughly 5 – 10% lower than the center wind speed. Therefore, the estimated growth rates of oblique waves in this study may be slightly underestimated.

4. Periodically Modulated Wind

4.1. Overview

[41] In this section, we present the results from controlled laboratory experiments to investigate the response of short

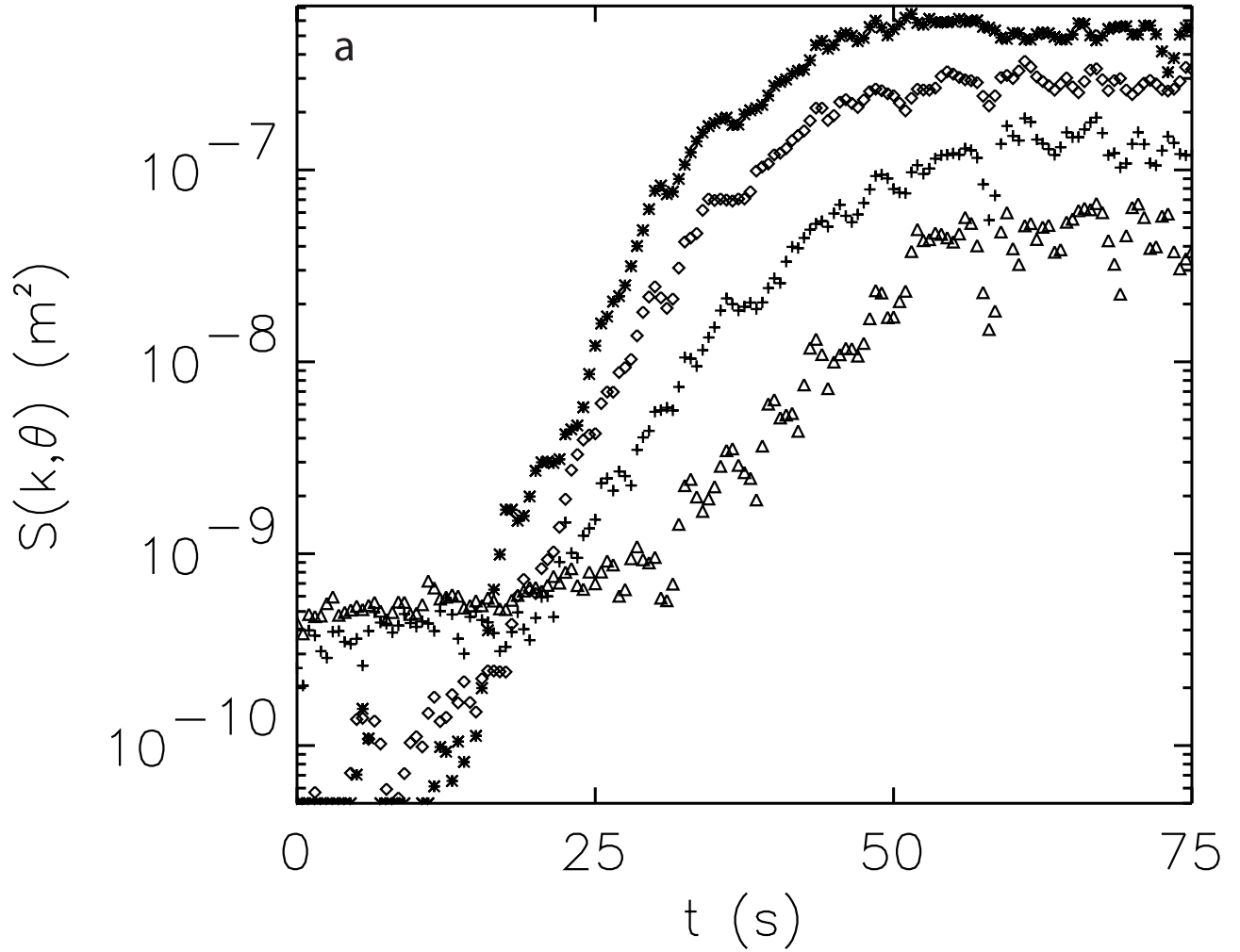


Figure 6. Time series of wave number slope spectrum in four directional ranges relative to the wind: * $0 \pm 15^\circ$, $\diamond 30 \pm 15^\circ$, + $60 \pm 15^\circ$, and $\triangle 90 \pm 15^\circ$. Wind speed 4.5 m s^{-1} . The spectrum is integrated over the wave number range described below: (a) $70\text{--}140$, (b) $175\text{--}245$, (c) $280\text{--}350$, (d) $350\text{--}455$, and (e) $525\text{--}700 \text{ rad m}^{-1}$.

wind waves under periodically modulated wind forcing. The two extreme cases of very long and very short modulation periods are trivial. If the modulation period is much shorter than the relaxation timescale of the waves, the variability of the wave spectrum is small since waves do not have time to respond to the forcing. At the other extreme, if the modulation period is much longer than the relaxation timescale, waves are able to follow the forcing without much deviation from their equilibrium condition corresponding to the instantaneous wind forcing. In between these two extremes lies an interesting range where the wind forcing and the wave response are not in phase. For this reason, the modulation periods of the experiment were chosen to be 10 and 20 s, which are roughly the relaxation timescales of short wind waves measurable with the SLSG. These timescales are also relevant for the modulation of wind by dominant ocean swells.

[42] At each modulation period, two mean wind speeds were used and sinusoidal modulation was added. The wave number slope spectra were boxcar averaged over 1 s and then phase averaged over many modulation cycles. The results were further averaged over certain wave number

ranges, described on top of each figure, in order to improve the statistical accuracy. Although the waves in different directions may respond differently to changing wind, we only present the along-wind wave number slope spectrum here. The response of oblique waves appeared to be similar to that of the along-wind waves but the results were too noisy to make any quantitative conclusions.

4.2. Wave Spectrum Versus Wind Speed

[43] We first present the response of the along-wind wave number slope spectrum to the modulated wind speed with a 10 s period in Figure 9. The results at steady winds are also shown with asterisks. Since waves grow and decay at a finite rate, the wave spectra are not in phase with the wind speed but lag behind it, and appear as hysteresis loops in the figure. The spectrum is higher when the wind is decreasing; hence, the spectrum always follows the hysteresis loop in the counterclockwise direction in time. Under all experimental conditions the time variation of the wind speed was almost perfectly sinusoidal in response to the modulated fan speed [Uz *et al.*, 2002]. However, the time variation of the wave spectrum was not necessarily sinusoidal. Therefore,

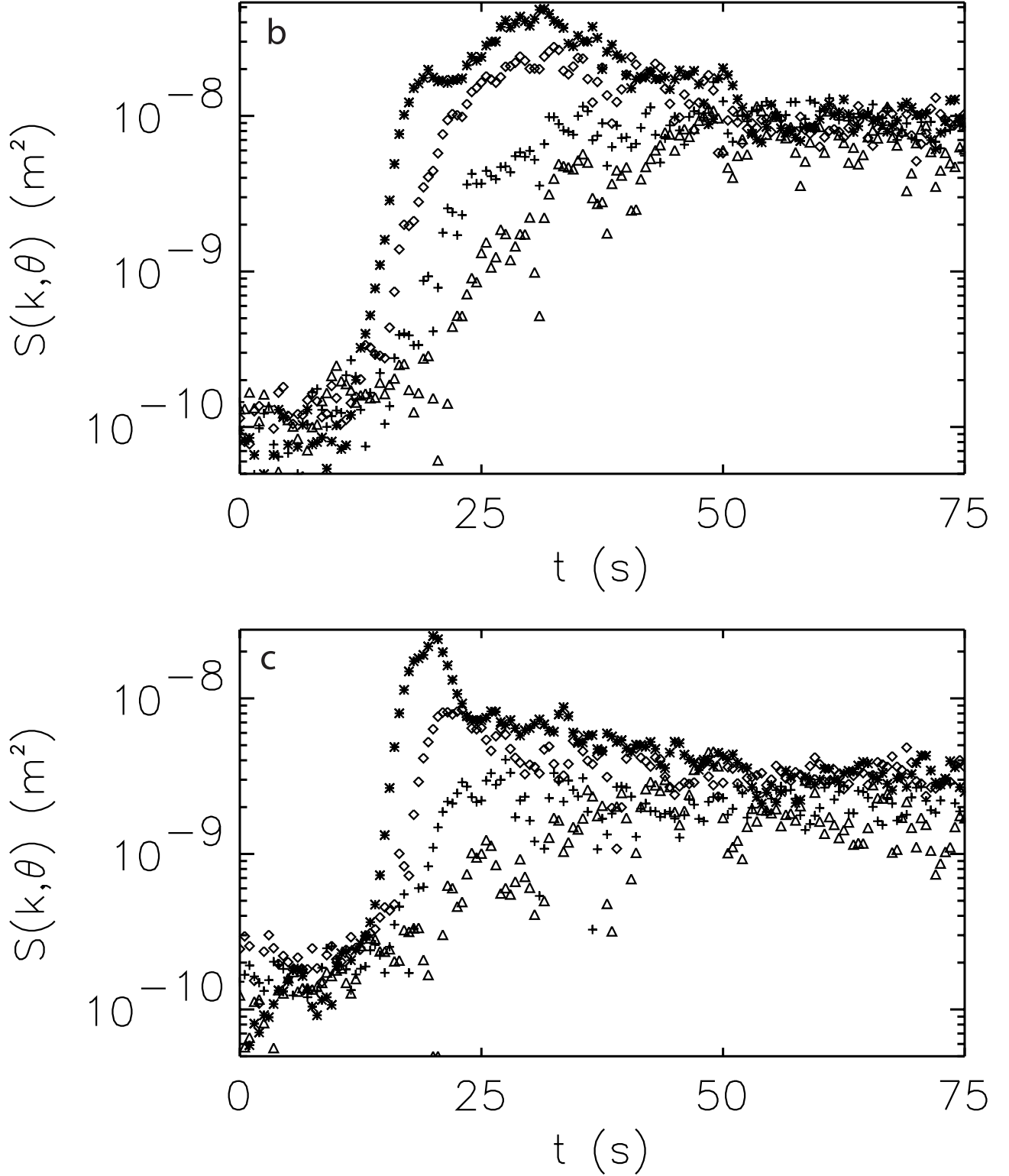


Figure 6. (continued)

the hysteresis loops do not always appear as a perfect ellipsoid. At higher mean wind speeds the hysteresis loops are slightly narrower. This is because the relaxation time-scale of a particular wave number component decreases with wind speed. The relationship between the mean wind speed and the mean wave spectrum for the modulated cases

is indicated by open squares. They are almost in line with the steady experimental data. Therefore, within the parametric range of this experiment the wind modulation does not seem to cause any significant bias.

[44] The results with 20 s modulation are shown in Figure 10. Now the width of the hysteresis loop is significantly

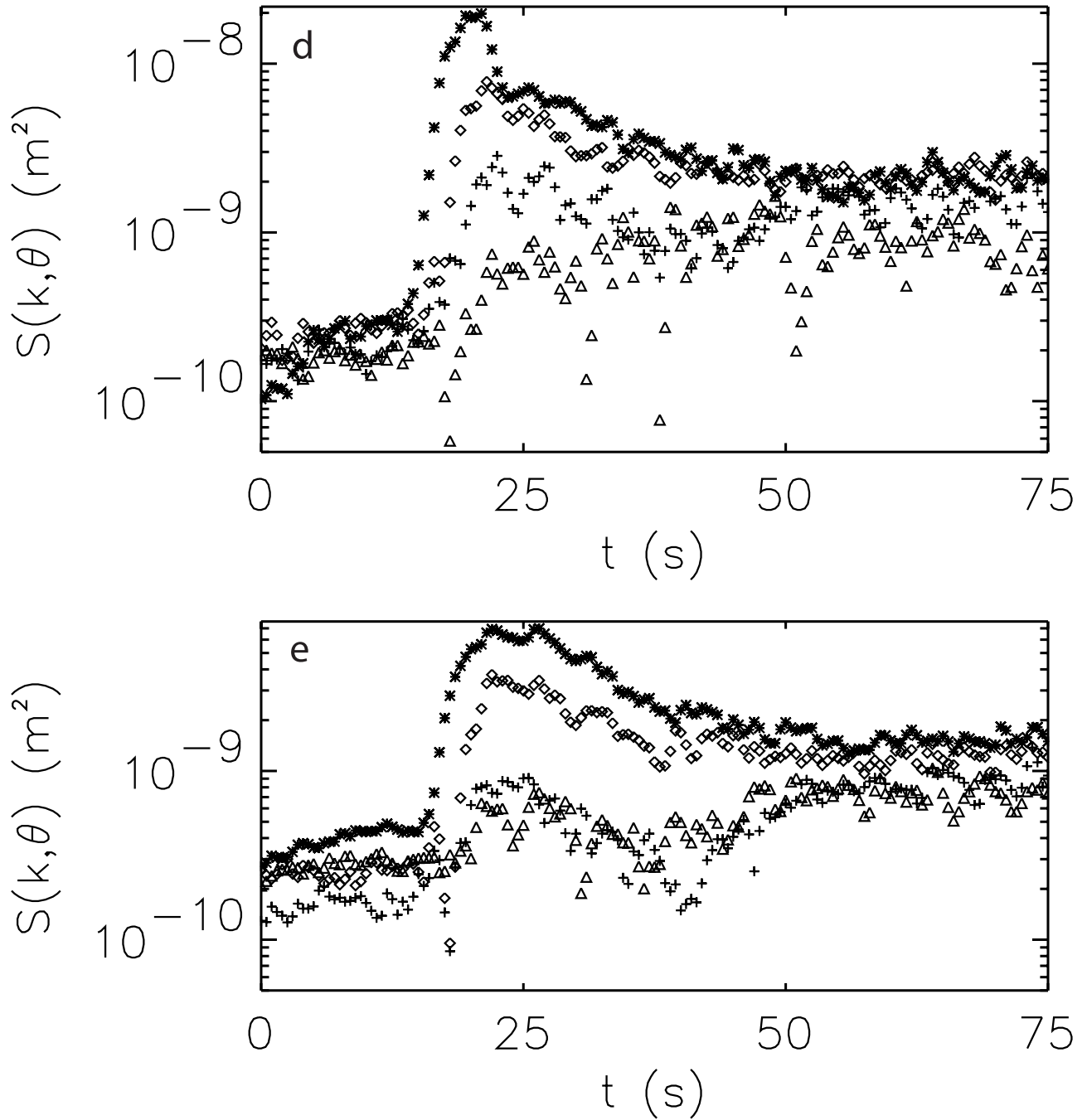


Figure 6. (continued)

reduced. In fact, most of the loops are narrower than the 95% confidence level and therefore are not well defined. This is simply because waves have more time to adjust to the changing wind conditions. Again, the relationship between the time-averaged wind speed and the wave spectrum under modulated wind is consistent with that under steady wind.

4.3. Wave Spectrum Versus Wind Friction Velocity

[45] Under transient wind forcing the relationship between the wind stress and the wind speed is not unique. This is because a significant part of the wind stress is supported by the wind waves rather than the viscous stress.

If the surface wave field is not in equilibrium with the instantaneous wind forcing, the relationship between the wind speed and the wind stress is also different from that under steady winds. Then, the hysteresis behavior of the wave spectrum should also depend on which variable is chosen to represent the wind forcing.

[46] When the along-wind wave spectra are plotted against the wind friction velocity instead of the wind speed, the hysteresis is much reduced as shown in Figure 11. This is qualitatively a reasonable result because when the wind speed is increasing the wave field is lower than its equilibrium value corresponding to the instantaneous wind speed. Therefore, the wind stress is also expected to be lower than

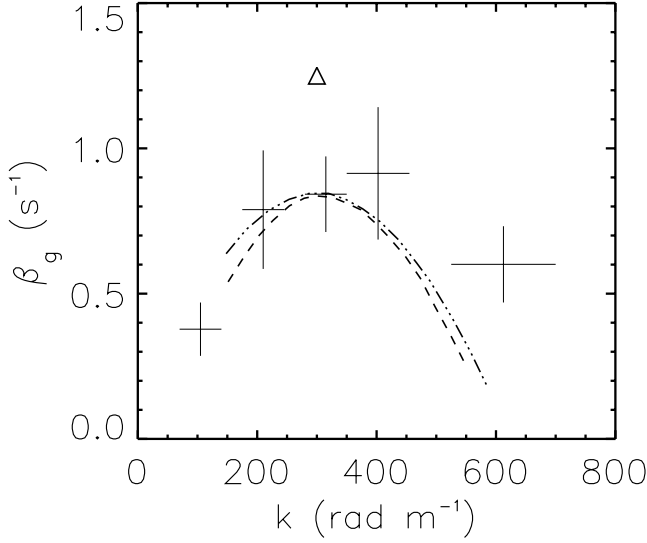


Figure 7. Measured growth rate of along-wind wave slope spectrum. Data from this study are shown by crosses at wind speed 4.5 m s^{-1} and friction velocity $0.15\text{--}0.19 \text{ m s}^{-1}$. Horizontal extent of the crosses indicates range of wave numbers averaged. Vertical extent of the crosses indicates uncertainty of the estimates. Triangle is measured growth rate by *Kawai* [1979] at friction velocity 0.170 m s^{-1} . Theoretical estimates of growth rate by *Kawai* [1979] and *van Gastel et al.* [1985] are shown by dash-dot-dot line and dashed line, respectively, at friction velocity 0.170 m s^{-1} .

the value under steady wind forcing. On the other hand, the wind stress should be higher when the wind is decreasing. Consequently, if the instantaneous wind friction velocity is plotted against the instantaneous wind speed, it also shows a hysteresis loop, as shown in Figure 12.

[47] In summary, the phase of the modulation of the wind friction velocity is behind that of the wind speed, and the phase of the modulation of the wave spectrum is further behind that of the wind friction velocity.

4.4. Relaxation Rate

[48] When wind waves are under modulated wind forcing, do they respond to the instantaneous wind speed or the instantaneous wind stress? How quickly do they follow the wind forcing? To answer these questions, we attempt to estimate the relaxation rate of the waves in response to both the modulated wind speed and the modulated wind stress.

[49] Let us assume that the wave spectrum at a particular wave number is governed by

$$\frac{DS}{Dt} = \beta_g(v)S - \alpha(v)S^n \quad (4)$$

under a particular wind forcing, denoted by v , which can be the wind speed (u), the wind friction velocity (u_*), or some other quantity. Here, β_g is the linear growth rate (i.e., the linear wind input rate minus the viscous dissipation rate), α is the nonlinear dissipation rate with n indicating the degree of nonlinearity. The differential operator $\frac{D}{Dt}$ applies to the time rate of change following the wave packet. This equation assumes that the wave spectrum at a particular

wave number is not influenced by those at different wave numbers, that is, the nonlinear wave interaction is negligible.

[50] The actual physical mechanisms of the dissipation of short wind waves may include wave breaking, interaction between waves and subsurface turbulence, etc. Some of the mechanisms are poorly understood and cannot be quantified accurately. Here, we simply hypothesize that the combined effect of all the dissipation mechanisms (except for the viscous dissipation) is a nonlinear function of the spectrum S with an unknown power of n . Furthermore, if the wind input is not strictly linear in S , the nonlinear correction to the wind input is also included in $\alpha(v)S^n$.

[51] When the wave spectrum is in equilibrium, we may set

$$0 = \beta_g(v)S_{eq}(v) - \alpha(v)[S_{eq}(v)]^n \quad (5)$$

where $S_{eq}(v)$ is the equilibrium spectrum as a function of the wind parameter v . If the spectrum S is slightly different from S_{eq} ,

$$S = S_{eq} + S', \quad |S'| \ll S_{eq} \quad (6)$$

then (4) is linearized in S' to yield

$$\frac{DS}{Dt} = -\beta(v)(S - S_{eq}(v)), \quad \beta \equiv \beta_g(v)(n - 1). \quad (7)$$

Hence, the spectrum approaches to the equilibrium state with the time rate of β , which is called the “relaxation rate.” The relaxation rate is related to the wave growth rate in a simple manner. For example, if the nonlinear dissipation

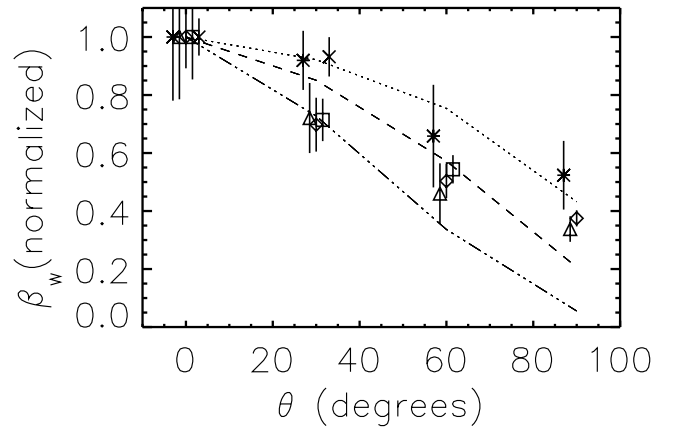


Figure 8. Wind input rate (growth rate plus viscous dissipation rate) at different wave directions θ normalized by its along-wind value. The results are averaged over $\theta = 0 \pm 15^\circ$, $30 \pm 15^\circ$, $60 \pm 15^\circ$, and $90 \pm 15^\circ$. Some data points are slightly shifted horizontally for clarity. The vertical bars indicate uncertainties of the estimates. Wind speed is 4.5 m s^{-1} and friction velocity is $0.15\text{--}0.19 \text{ m s}^{-1}$. The wind input rate is averaged over the wave number range of stars 70–140, triangles 175–245, diamonds 280–350, squares 350–455, and tilted crosses 525–700 rad m^{-1} . The lines represent $\cos^p(\theta)$ dependence with $p = 0.5$ (dot), 1.0 (dash), and 2.0 (dash-dot).

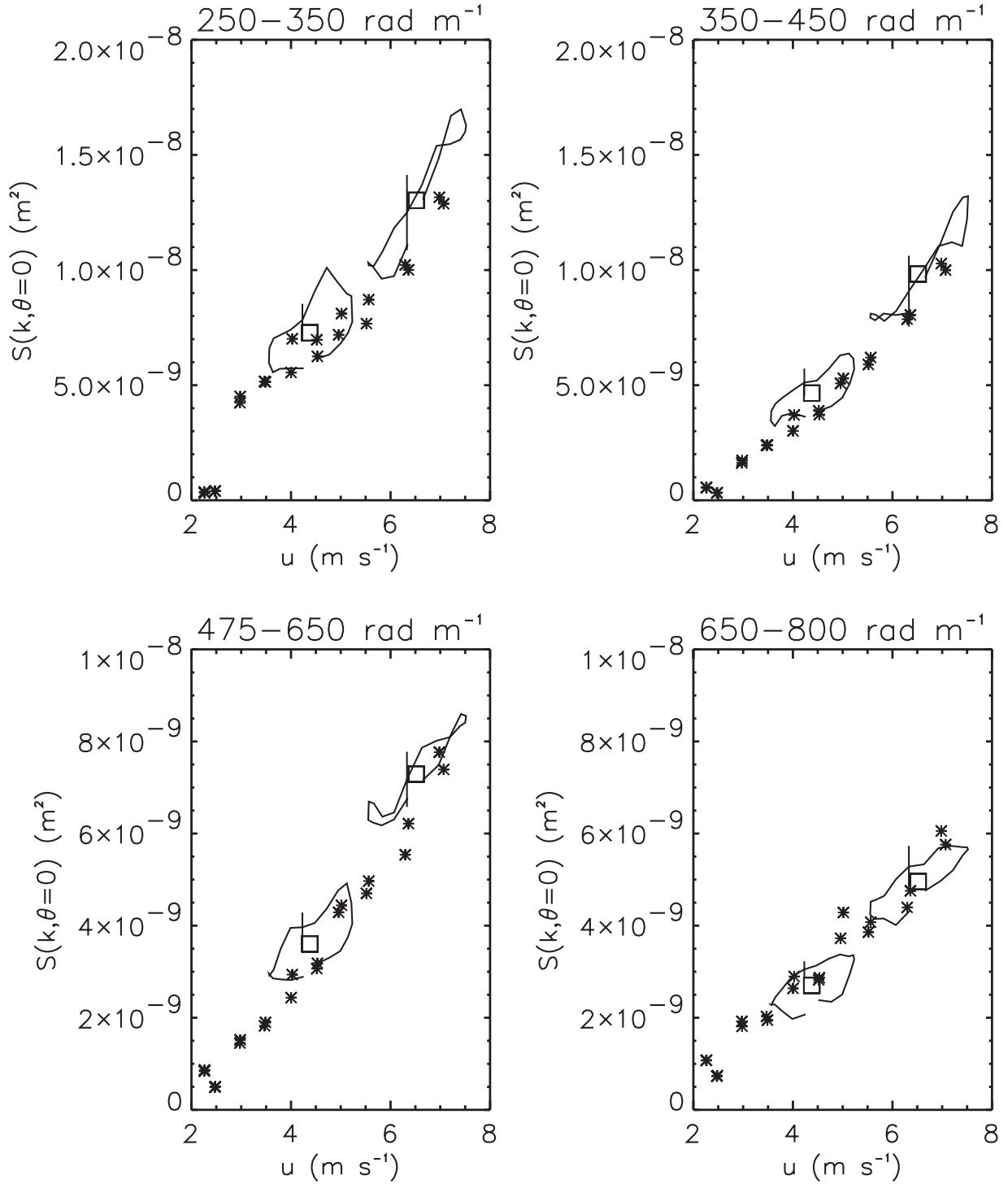


Figure 9. Along-wind wave number slope spectrum versus wind speed under modulated wind forcing. Modulation period is 10 s. The spectrum is averaged over the wave number range indicated on top of each figure. Vertical bars indicate 95% confidence level. Open squares represent mean over a modulation period. Asterisks are results under steady wind forcing.

term is quadratic ($n = 2$) or cubic ($n = 3$), $\beta = \beta_g$ or $\beta = 2\beta_g$, respectively. This approach was applied in many previous studies of short wind wave modulations due to ocean swells, internal waves, and other variable forcing [e.g., Hara and Plant, 1994].

[52] In our experiment, the spatial dependence is weak, and $\frac{D}{Dt}$ can be replaced by $\frac{d}{dt}$. If the wind parameter is modulated such that

$$v = \bar{v} + \tilde{v}, \quad |\tilde{v}| \ll \bar{v}, \quad (8)$$

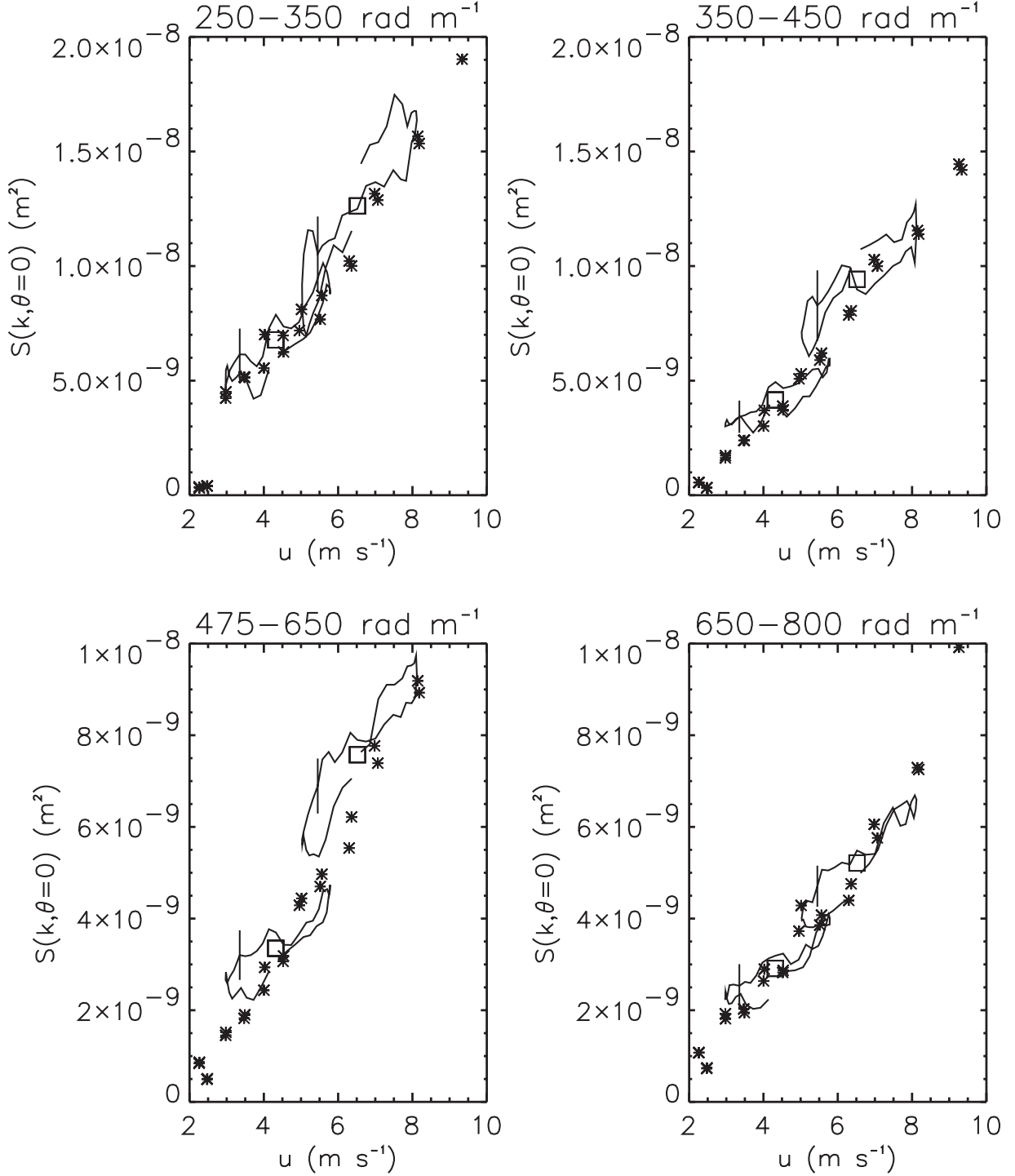


Figure 10. Same as Figure 9, but with a modulation period of 20 s.

the equation for the modulation of the wave spectrum becomes

$$\frac{d\tilde{S}}{dt} = -\beta \left(\tilde{S} - \frac{dS_{eq}}{dv} \tilde{v} \right) \quad (9)$$

where

$$\tilde{S} = S - S_{eq}(\tilde{v}). \quad (10)$$

The quantity $\frac{dS_{eq}}{dv}$ can be obtained empirically from the stationary wind experiments reported by *Hara et al.* [1997]. Therefore, if \tilde{v} and \tilde{S} are known from the measurements, we may estimate the relaxation rate β . Since the available data contain large scatter, we instead solve equation (9) using the measured wind parameter \tilde{v} and different values of β and seek the best fit (by seeking the least mean square errors) between the prediction and the observation of \tilde{S} . The results are shown by solid ellipses in Figure 13 for the wind speed and Figure 14 for the wind friction velocity. We also

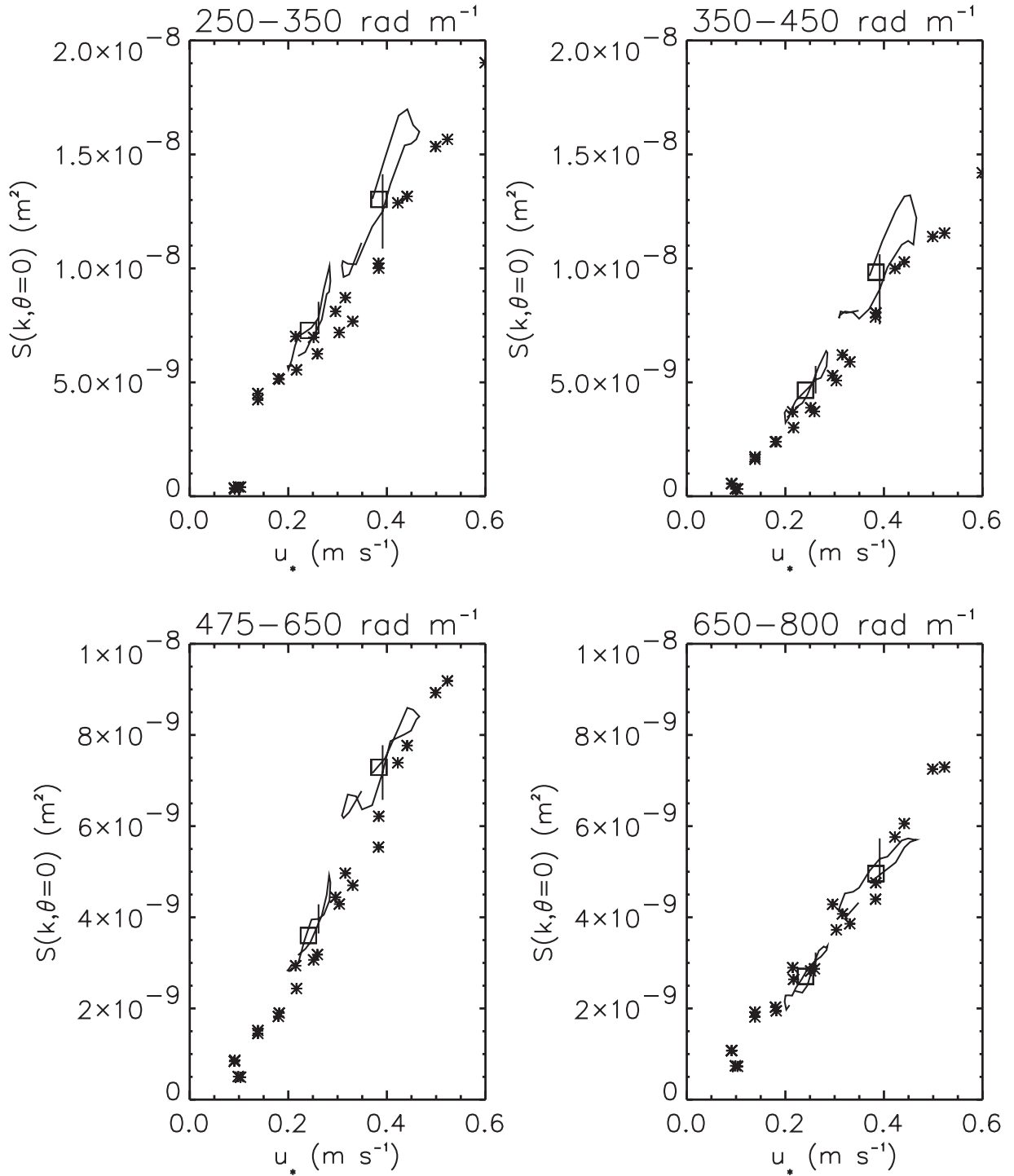


Figure 11. Along-wind wave number slope spectrum versus wind friction velocity under modulated wind forcing. Modulation period is 10 s. The spectrum is averaged over the wave number range indicated on top of each figure. Vertical bars indicate 95% confidence level. Open squares represent mean over a modulation period. Asterisks are results under steady wind forcing.

simulate how the wave spectrum should respond if the relaxation rate is equal to the wave growth rate that was estimated in the previous section. Such results are shown by dotted ellipses in Figures 13 and 14.

[53] When the wind speed is chosen as the wind parameter (Figure 13), the best-fit hysteresis loops (solid ellipses)

are wider than the simulated loops (dotted ellipses) with the relaxation rate being equal to the wave growth rate, except at the highest wave number range. The best-fit relaxation rates are 0.12, 0.30, 0.20, and 0.20 s^{-1} , for the wave number ranges of 250–350, 350–450, 475–650, and 650–800 rad m^{-1} , respectively, while the measured growth rates

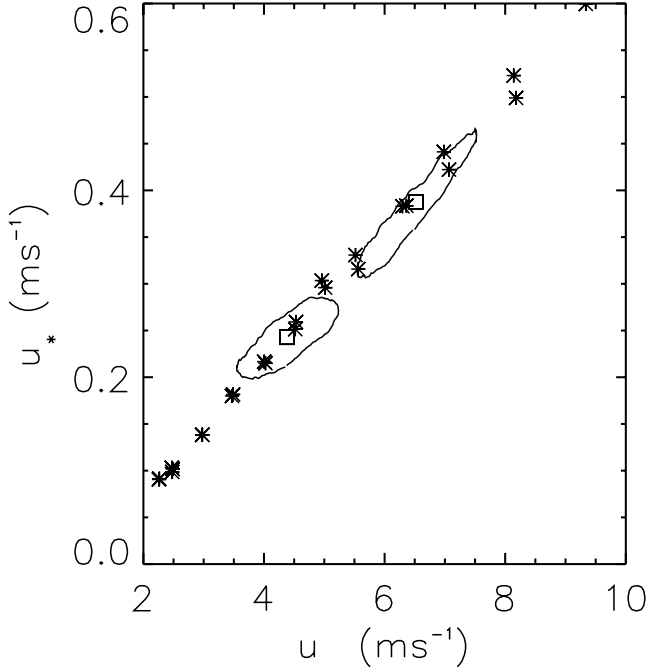


Figure 12. Wind friction velocity versus wind speed under modulated wind forcing. Modulation period is 10 s. Open squares represent mean over a modulation period. Asterisks are results under steady wind forcing.

are 0.89, 0.81, 0.68, and 0.29 s^{-1} , respectively. Therefore, if the waves are responding to the instantaneous wind speed, longer waves are responding at a much slower rate than that predicted from the relaxation theory. Only at the highest wave number range, the observation is roughly consistent with the prediction. If we assume that the relaxation rate is twice the growth rate or larger (i.e., the power n of the nonlinear dissipation term in (4) is 3 or larger), its difference from the best-fit relaxation rate further increases.

[54] Next, if the wind friction velocity is chosen as the wind parameter (Figure 14), the best-fit hysteresis loops are narrower than the simulated hysteresis loops except at the lowest wave number range. The best-fit relaxation rates are 0.79, 1.98, 1.32, and 1.35 s^{-1} , for the wave number ranges of 250–350, 350–450, 475–650, and 650–800 rad m^{-1} , respectively. Therefore, observed modulation of longer waves is roughly consistent with the relaxation model prediction with the relaxation rate being equal to the growth rate, but shorter waves are responding much too quickly. If we assume that the relaxation rate is twice the growth rate or larger, the agreement improves for shorter waves but becomes worse for longer waves.

[55] With these observations we may tentatively conclude that very short gravity-capillary waves respond more to the instantaneous wind speed than to the wind stress, while longer waves respond more to the instantaneous wind stress than the wind speed, as long as the relaxation theory is valid and the relaxation rate is identical to the growth rate. It does not appear that the relaxation rate is much larger than the growth rate since the overall agreement between the observation and the prediction becomes worse when the relaxation rate is assumed to be twice the

growth rate or larger. Therefore, the nonlinear dissipation term in (4) is more likely to be quadratic than cubic or stronger. Of course, further investigations with a wider range of parameters are necessary to make a more conclusive statement.

[56] It has been shown earlier that a significant fraction of the gravity-capillary wave spectrum is in the bound wave mode rather than in the free wave mode (see Figure 2g). The response of the bound waves to changing wind forcing is determined by the response of the dominant waves. Therefore, the fluctuations in the spectrum at high wave numbers may have two independent components, one corresponding to the relaxation of the free waves and the other determined by the relaxation of the bound waves. However, the presence of the bound waves does not necessarily invalidate our relaxation rate estimates, because the dominant waves including their higher harmonics are subject to a much longer relaxation timescale and are hardly modulated. Then, the bound wave contribution is merely a constant added to both the instantaneous and the equilibrium values of the free wave contribution, and as such has little effect on the relaxation rate measurements or estimates.

4.5. Discussion on the Modulation Results

[57] Why do longer waves respond to the instantaneous wind stress while shorter waves respond to the instantaneous wind speed? To answer this question, let us first consider what wind quantity is the most relevant to the forcing of a particular wave component. Recently, several theories have been proposed suggesting that in the presence of longer waves shorter waves feel reduced wind forcing due to *sheltering*. Long waves remove momentum from wind, in the form of wave-induced stress (form drag), thus leave a smaller turbulent stress to force growth of the short waves. This process was incorporated into a model of the roughness of the sea surface developed by *Makin et al.* [1995] and *Makin and Kudryavtsev* [1999]. Quantitative evidence of the sheltering effect has been reported by *Chen and Belcher* [2000], who show that wind-forced growth of short wind waves in the presence of a long paddle-generated wave is reduced by sheltering by the long wave. The idea of sheltering is also incorporated in the theory of the equilibrium wave spectrum under strong wind forcing by *Hara and Belcher* [2002].

[58] According to the sheltering theory, the growth of a particular wave number component is determined by the local turbulent stress, which is defined as the total wind stress minus the stress supported by waves at lower wave numbers. In the case of our modulation experiment, the dominant waves are subject to the total wind stress, and progressively lower wind stress is applied to shorter waves. It is therefore reasonable that relatively longer waves respond to the total wind stress in our experiment, because their local stress is not very different from the total stress. On the other hand, the local wind stress applied to the smallest waves should be almost the same as the skin friction, that is, the stress supported by viscosity at the water surface. Recent observational study by *Banner and Peirson* [1998] reports that the relationship between the wind speed and the skin friction velocity is roughly linear regardless of the stage of the wave development. Then, the skin friction is expected to

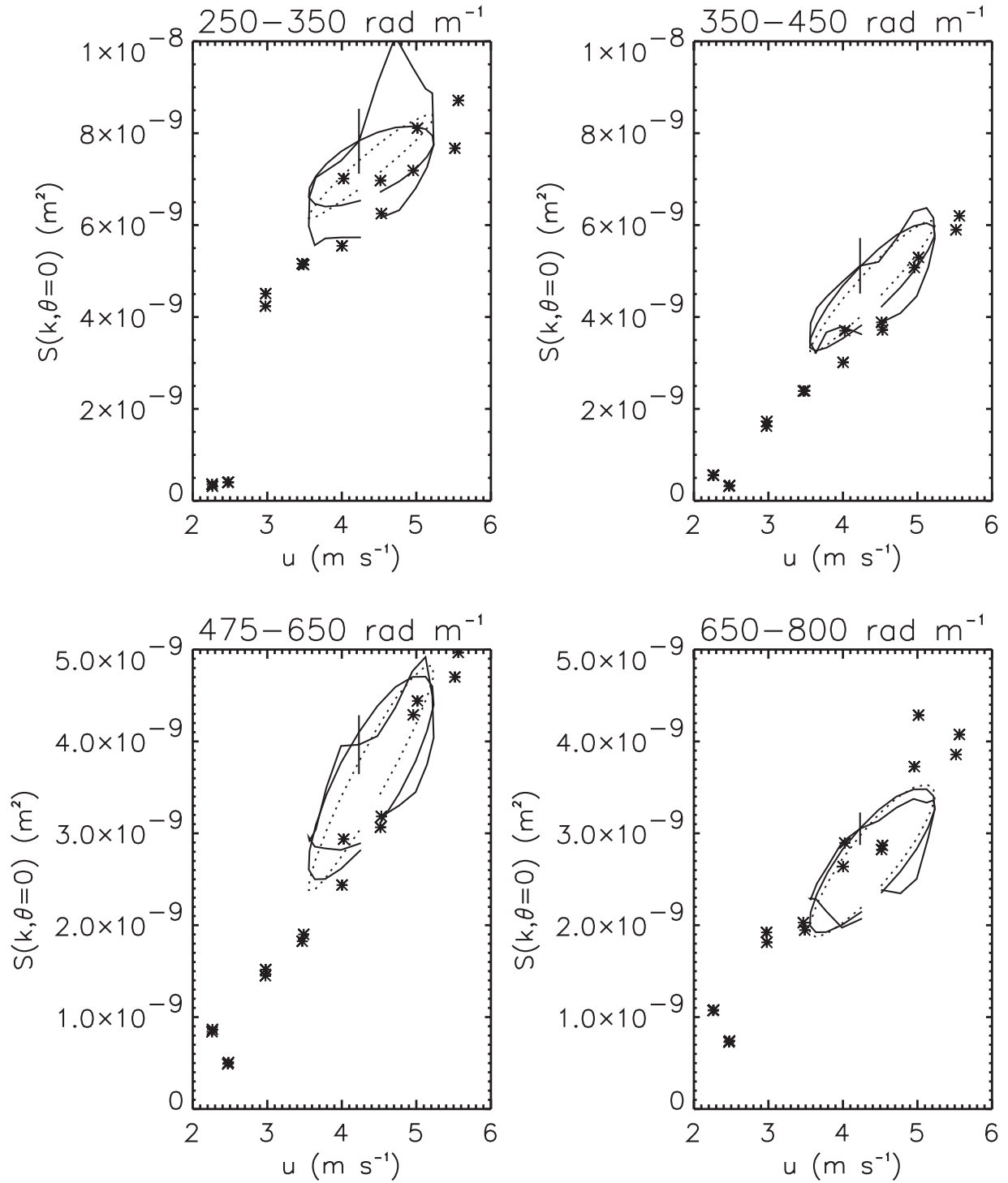


Figure 13. Along-wind wave number slope spectrum versus wind speed under modulated wind forcing. Modulation period is 10 s. The spectrum is averaged over the wave number range indicated on top of each figure. Vertical bars indicate 95% confidence level. Asterisks are results under steady wind forcing. Solid ellipsoids are hysteresis loops calculated with the best-fit relaxation rate estimates. Dotted ellipsoids are hysteresis loops calculated using the measured wave growth rate.

be more closely related to the wind speed rather than the total wind stress. This fact may explain why very short wind waves appear to respond more to the instantaneous wind speed than the wind stress in our experiment.

[59] In summary, our modulation observations seem to support the idea of “sheltering,” at least qualitatively. More

quantitative tests of the sheltering theory are given in the companion paper [Uz *et al.*, 2002].

5. Conclusion

[60] Controlled laboratory experiments were conducted to investigate the dynamics of short wine waves under tran-

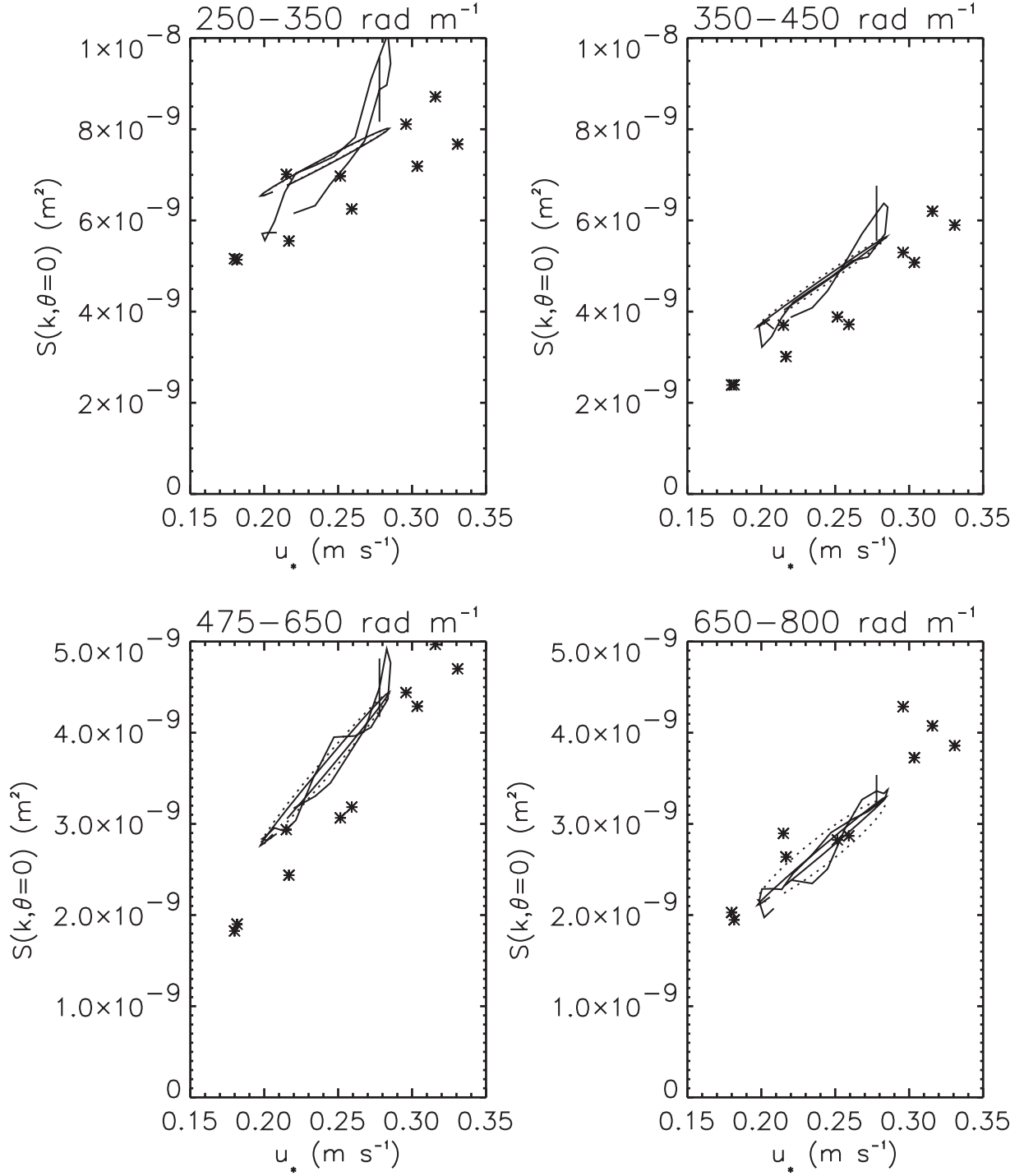


Figure 14. Along-wind wave number slope spectrum versus wind friction velocity under modulated wind forcing. Modulation period is 10 s. The spectrum is averaged over the wave number range indicated on top of each figure. Vertical bars indicate 95% confidence level. Asterisks are results under steady wind forcing. Solid ellipsoids are hysteresis loops calculated with the best-fit relaxation rate estimates. Dotted ellipsoids are hysteresis loops calculated using the measured wave growth rate.

sient wind forcing. Using a SLSG, we could directly estimate the three-dimensional wave number frequency slope spectrum of short wind waves. This allowed us to distinguish wavelengths and wave propagating directions, in contrast to previous laboratory measurements that yielded only the frequency spectrum.

[61] In the first set of experiments, the evolution of wind waves from the initial generation to the final saturation was investigated under rapidly starting wind. Our observations clearly suggest that at the initial stage waves in a wide wave number range (both in magnitude and direction) grow exponentially and independently at their own growth rates.

The initial wavelet appears first because they correspond to the wave number with the maximum growth rate. For a given wavelength the growth rate decreases monotonically as the angle θ between the wave and wind directions increases, although it does not seem to follow the $\cos^p\theta$ dependence with a particular p .

[62] After the initial wavelets attain their maximum value, the peak wave number and peak frequency start to downshift. This process does not seem to be caused by the “period doubling,” which was theoretically predicted by Janssen [1986]. Toward the later stage of the wave evolution, the contribution of bound wave components to the wave number frequency spectrum becomes as important as that of free wave components.

[63] The second sets of experiments were conducted under periodically modulated wind speed, with a modulation period of 10 or 20 s. The modulation of the wind stress is slightly behind that of the wind speed, and the modulation of the short wind wave spectrum is further behind that of the wind stress. The results have been compared with the prediction based on the relaxation theory, with the relaxation rate being equal to the measured wave growth rate. If we assume that waves respond to the instantaneous wind speed, the observed wave modulation is consistent with the prediction at very high wave numbers, but is far behind the prediction at lower wave numbers. If the effective relaxation rates are estimated based on the observations, the results are as small as 1/8 of the measured growth rates. On the other hand, if waves are assumed to respond to the instantaneous wind stress, observations and predictions are roughly consistent at lower wave numbers, but at very high wave numbers the prediction seems to overestimate the delay. From these observations we may tentatively conclude that longer waves respond more to the wind stress than to the wind speed, while shorter waves respond more to the wind speed than to the wind stress. This conclusion can be qualitatively explained in terms of the sheltering effect. Of course, more direct observations of pressure and turbulent stresses near the water surface are needed in order to fully understand the wind forcing of short wind waves under time-transient conditions.

[64] Our results appear to support the idea of relaxation theory and use of the wave growth rate as a proxy for the relaxation rate. However, the same relaxation theory may yield very different results depending on which parameter (wind stress or wind speed) is chosen as the wind forcing parameter. Further studies, both experimental and theoretical, will be necessary to clarify the true wind forcing parameter for a particular wave component in the presence of a wide spectrum of waves.

[65] **Acknowledgments.** This work was supported by the U.S. National Science Foundation (award OCE9402241). Additional support was provided by the U.S. Office of Naval Research (awards N00014-95-10116 and N00014-96-10510). We thank the National Water Research Institute and especially D. Beasley and J. Cooper for support during the experiment. Finally, we report with great sadness that one of our coauthors, Erik Bock, passed away in 2001 while this paper was still under review. Erik's contributions (especially the development of the scanning laser slope gauge) were invaluable to this study as well as to numerous other air–sea interaction studies in which he was involved.

References

- Autard, L., and G. Caulliez, Effect of a wind gust on a fully developed wave field, in *The Air–Sea Interface: Radio and Acoustic Sensing, Turbulence and Wave Dynamics*, edited by M. A. Donelan et al., Rosenstiel Sch. of Mar. and Atmos. Sci., Univ. of Miami, Miami, Fla., 1996.
- Banner, M. L., and W. L. Peirson, Tangential stress beneath wind-driven air–water interfaces, *J. Fluid Mech.*, **364**, 115–145, 1998.
- Bock, E. J., and T. Hara, Optical measurements of capillary-gravity wave spectra using a scanning laser slope gauge, *J. Atmos. Oceanic Technol.*, **12**, 395–403, 1995.
- Caulliez, G., and F. Collard, Three-dimensional evolution of wind waves from gravity-capillary to short gravity range, *Eur. J. Mech. B, Fluids*, **18**, 389–402, 1999.
- Chen, G., and S. E. Belcher, Effects of long waves on wind-generated waves, *J. Phys. Oceanogr.*, **30**, 2246–2256, 2000.
- Dorman, C., and E. Mollo-Christensen, Observations of the structure on moving gust patterns over a water surface (“cat’s paws”), *J. Phys. Oceanogr.*, **3**, 120–132, 1973.
- Hara, T., and S. E. Belcher, Wind forcing in the equilibrium range of wind-wave spectra, *J. Fluid Mech.*, **470**, 223–245, 2002.
- Hara, T., and W. J. Plant, Hydrodynamic modulation of short wind-wave spectra by long waves and its measurement using microwave backscatter, *J. Geophys. Res.*, **99**, 9767–9784, 1994.
- Hara, T., E. J. Bock, and D. Lyzenga, In situ measurements of capillary-gravity wave spectra using a scanning laser slope gauge and microwave radars, *J. Geophys. Res.*, **99**, 12,593–12,602, 1994.
- Hara, T., E. J. Bock, and M. Donelan, Frequency-wavenumber spectrum of wind-generated capillary-gravity waves, *J. Geophys. Res.*, **102**, 1061–1072, 1997.
- Hara, T., E. J. Bock, J. B. Edson, and W. R. McGillis, Observations of short wind waves in coastal waters, *J. Phys. Oceanogr.*, **28**, 1425–1438, 1998.
- Hwang, P. A., D. B. Trizna, and J. Wu, Spatial measurements of short wind waves using a scanning slope sensor, *Dyn. Atmos. Oceans*, **20**, 1–23, 1993.
- Hwang, P. A., S. Atakturk, M. A. Sletten, and D. B. Trizna, A study of the wavenumber spectra of short water waves in the ocean, *J. Phys. Oceanogr.*, **26**, 1266–1285, 1996.
- Jähne, B., and K. S. Riemer, Two-dimensional wave number spectra of small-scale water surface waves, *J. Geophys. Res.*, **95**, 11,531–11,546, 1990.
- Janssen, P. A. E. M., The period-doubling of gravity-capillary waves, *J. Fluid Mech.*, **172**, 531–546, 1986.
- Kawai, S., Generation of initial wavelets by instability of a coupled shear flow and their evolution to wind waves, *J. Fluid Mech.*, **93**, 661–703, 1979.
- Larson, T. R., and J. W. Wright, Wind generated gravity-capillary waves: Laboratory measurements of temporal growth rates using microwave backscatter, *J. Fluid Mech.*, **70**, 417–436, 1975.
- Makin, V. K., and V. N. Kudryavtsev, Coupled sea surface-atmosphere model, 1, Wind over waves coupling, *J. Geophys. Res.*, **104**, 7613–7623, 1999.
- Makin, V. K., V. N. Kudryavtsev, and C. Mastenbroek, Drag of the sea surface, *Boundary Layer Meteorol.*, **73**, 159–182, 1995.
- Melville, W. K., R. Shear, and F. Veron, Laboratory measurements of the generation and evolution of Langmuir circulations, *J. Fluid Mech.*, **364**, 31–58, 1998.
- Uz, B. M., M. A. Donelan, T. Hara, and E. J. Bock, Laboratory studies of the effect of short wind waves on wind stress, *Boundary Layer Meteorol.*, **102**, 301–331, 2002.
- van Gastel, K., P. A. E. M. Janssen, and G. J. Komen, On phase velocity and growth rate of wind-induced gravity-capillary waves, *J. Fluid Mech.*, **161**, 199–216, 1985.
- Weissman, D. E., W. J. Plant, and S. Stolte, Response of microwave cross sections of the sea to wind fluctuations, *J. Geophys. Res.*, **101**, 12,149–12,161, 1996.
- Zhang, X., Capillary-gravity and capillary waves generated in a wind wave tank: Observations and theories, *J. Fluid Mech.*, **289**, 51–82, 1995.

E. J. Bock, Interdisciplinary Center for Scientific Computing, University of Heidelberg, Heidelberg, Germany.

M. A. Donelan, Rosenstiel School of Marine and Atmospheric Science, University of Miami, Miami, FL, USA.

T. Hara, Graduate School of Oceanography, University of Rhode Island, Narragansett, RI, USA. (THARA@URI.EDU)

B. M. Uz, Earth System Science Interdisciplinary Center, University of Maryland, College Park, MD, USA.